

Nitrogen-seeded divertor detachment in TCV L-mode plasmas

O. Février¹, C. Theiler¹, J. R. Harrison³, C. K. Tsui^{2,1}, K. Verhaegh^{4,1}, C. Wüthrich¹, J.A. Boedo², H. De Oliveira¹, B. P. Duval¹, B. Labit¹, B. Lipschultz⁴, R. Maurizio¹, H. Reimerdes¹, the TCV Team^a and the EUROfusion MST1 Team^b

¹École Polytechnique Fédérale de Lausanne (EPFL), Swiss Plasma Center (SPC), CH-1015 Lausanne, Switzerland.

²University of California-San Diego, La Jolla, California 92093, USA.

³CCFE, Culham Science Centre, Abingdon, OX14 3DB, Oxon UK.

⁴York Plasma Institute, University of York, Heslington, York, YO10 5DQ, UK.

^aSee the author list of S. Coda et al 2019 *Nucl. Fusion* **59** 112023.

^bSee the author list of B. Labit et al 2019 *Nucl. Fusion* **59** 086020.

E-mail: olivier.fevrier@epfl.ch

Abstract. Most of the detachment experiments done to date on the Tokamak à Configuration Variable (TCV), both in standard and alternative divertor geometries, focused on L-mode integrated core density ramps. In view of extending these studies to high-power, high-confinement regimes, where impurity seeding will be necessary for detachment, the properties of nitrogen seeded L-mode detachment in TCV are assessed here with the extensive set of edge and divertor diagnostics and similarities and differences with integrated core density ($\langle n_e \rangle$) ramp detachment experiments are elucidated. It is found that in high current, reversed field plasmas, detachment at the outer target is achieved with N₂-seeding and density ramps, with target heat flux reductions of up to 90%, while the inner target only detaches with seeding. The Scrape-Off Layer radiation fraction reaches values of 60-80% and in all situations, a stable radiator can form around the X-point. The most striking difference between seeding and density ramp is the behavior of the upstream quantities. During the $\langle n_e \rangle$ -ramp, a broadening of the upstream density profile (density “shoulder”) occurs, concurrent with the outer target ion flux roll-over, while no such behavior occurs during nitrogen seeded detachment. Separatrix density, electron temperature and pressure also evolve strongly with increasing density, and are largely unaffected by the injection of nitrogen. Comparison of upstream and target pressures reveals that, in all cases, the outer target ion flux reduction coincides with the development of a parallel gradient of the total pressure. Common to all cases is also a reduction of energy confinement time with detachment, although this effect is weak for seeding at relatively high density. Studying the impact of the ∇B -drift direction in both nitrogen seeding and core density ramps reveals that drifts mainly affect the behavior at the inner strike point, highlighting the need to include drift in edge transport simulations.

1. Introduction

In a tokamak, a large proportion of the input power leaves the confined plasma through perpendicular transport and enters the Scrape-Off Layer (SOL), where it is radiated or transported towards a narrow region of the machine wall. Due to material limitations, the operation of future devices such as ITER will require that target heat fluxes be less than 10 MW/m^2 [1, 2] for steady-state conditions. However, if unmitigated, target heat fluxes in ITER and DEMO are expected to be well above this value [3]. Therefore, it remains crucial to dissipate this incoming power before it is deposited upon the targets. Operation in a detached regime [4, 5, 6] is presently considered necessary, where most of the exhaust heat is dissipated as radiation, and where the plasma pressure along the field lines in the SOL develops strong parallel gradients. Detachment substantially reduces the target heat and particle fluxes, and the target temperature, which is important to reduce target erosion [7, 8]. The detachment process typically sets in at a target temperature below 5 eV [9, 10, 11]. In these conditions, the interaction of the plasma with neutrals becomes important, reducing target heat flux, temperature, and ion flux. This further reduction in temperature promotes the onset of volumetric momentum losses [12, 11], resulting in the formation of a pressure difference between the upstream location and the targets.

Often, the most convenient way to reach a detached regime is to raise the separatrix density $n_{e,sep}$, leading to lower target temperatures (as predicted by the two-point model [4]) and increased hydrogenic radiation. This is observed in experiments, such as Alcator C-Mod [13], ASDEX-Upgrade [10], DIII-D [14], JET [12], JT-60U [15] and TCV [16] where, above a certain density threshold, the ion flux to the target starts to decrease as $n_{e,sep}$ increases. For TCV in particular, such density ramps have been the main point of focus of the experiments on alternative divertor configurations [16, 17]. In these experiments, as well as in carbon machines in general, intrinsic carbon impurity ions play an important role. Increasing the upstream density changes the carbon source within the machine (resulting either from chemical and physical sputtering) hence increasing the power radiated by carbon, which can constitute up to 80% of the radiated power in detached plasmas, as seen in DIII-D [18] and TCV [11].

The approach of raising the separatrix density to reach detachment can, however, be detrimental to core confinement [19] and is subject to the Greenwald density limit in tokamaks [20]. Particularly in metal wall protected machines, other means are therefore explored to access detachment. One possible solution is to inject impurities, leading to volumetric radiation of the power in the edge region, the SOL and the divertor, and thus a reduction in the power reaching the divertor targets, which in turn facilitates access to a detached regime. For ITER and DEMO, a large fraction of the incoming power must be radiated (approximately 60-75% in ITER[21, 3, 22], and more than 95% of the heating power in DEMO[23, 3]). The main candidates for this task are the noble gases (Ne, Ar, Kr, Xe) or nitrogen (N, injected as N_2) [8, 24]. The selection of the impurity mix is dictated by their chemical and radiative properties together with several operational constraints. In ITER, while a high divertor radiation level will be necessary in order to access a (partially) detached regime and protect the divertor plates, operation with an available auxiliary heating power close to the L-H threshold imposes a radiator that does not lead to significant core radiation[3]. Taken further, the power provided by the α -heating in DEMO will require energy dissipation through radiation inside the separatrix too[3].

To study the physics of impurity seeded detachment on today's tokamaks, nitrogen (N) is a suitable choice. Its radiative properties are close to those of carbon, with a high radiative efficiency for the range of temperature typically encountered in the divertor region, yet remaining relatively low in the plasma core. In this article, we report on recent L-Mode N_2 -seeding detachment experiments performed on the Tokamak à Configuration Variable (TCV) [25] at EPFL and compare the findings to a detailed, quantitative analysis of line-averaged core density ($\langle n_e \rangle$) ramps. The goal of this article is to provide a detailed description of the main observations achieved in such plasmas and a critical assessment of the extensive set of edge/divertor diagnostics at TCV and their reliability in the different conditions. This work provides a comprehensive set of data for the validation of detachment simulations using 2D transport codes such as SOLPS-ITER [26] and SOLEDGE2D [27], and critical support for H-Mode experiments in conventional and alternative divertor configurations [28, 29], where N_2 -seeding is found to be necessary to achieve detachment. Most

of the experiments reported here are performed with reversed field (or “unfavorable ∇B ”), where the ∇B drift points away from the X-point, and high-current conditions, allowing to operate at high-density, favorable for detachment, without transitioning to Ohmic H-mode. However, in view of future H-mode detachment studies, which will most likely focus on forward field scenarios, the main changes with field direction in lower current, L-mode plasmas are also presented.

This paper is organized as follows. In section 2, we present the experimental setup, including the diagnostics used in this study, and describe the scenarios that will be compared. In section 3, we investigate the behavior of the target quantities, determined by Langmuir Probes and Infrared thermography, as we approach detachment by either increasing the line-averaged density $\langle n_e \rangle$ or injecting N_2 . In section 4, we focus on the power balance of these plasmas and show where, and to what extent, the power is radiated. In section 5, we study the behavior of the CIII and NII radiation front movement, and their ability to monitor the detachment state. In section 6, we discuss the evolution of the upstream separatrix quantities and SOL profiles, followed in section 7 by an assessment of the effect of detachment on core performance. The dependence of the detachment on field direction, in lower current plasmas and both for seeded and $\langle n_e \rangle$ -ramp experiments, is discussed in section 8. Summary and conclusion are presented in section 9.

2. Experimental setup

This work was performed on TCV [25], a medium size tokamak (major radius $R_0 = 0.88$ m, minor radius $a = 0.25$ m, $B_0 \approx 1.44$ T), with unique shaping capabilities. In figure 1, we plot the magnetic geometry used in this study, together with the gas valve locations and the spatial coverage of the diagnostics most relevant for this work. The radial positions of the two gas valves are indicated by the black rectangles in the left panel of figure 1. These valves employ a piezo-electric crystal with integrated flow measurement, providing calibrated flow rates [30]. Both valves are toroidally localized on the TCV floor. D_2 is injected through the outermost valves at a fueling rate controlled by a feedback loop based on the line-averaged density $\langle n_e \rangle$ measured by the central chord of the FIR (Far-InfraRed interferometer), also shown on the left panel of figure 1. For N_2 -seeded discharges, N_2 is injected through the innermost valve, following a prescribed ramp. The locations of the wall-embedded Langmuir Probes (LPs) [31, 32, 33] are indicated by red dots. They are operated with a triangular voltage sweep, ranging from -120V to +80 V, typically at a frequency of 330 Hz. Details

on the LP analysis can be found in Ref. [32]. The black lines in the left panel of figure 1 correspond to the lines of sight of a multi-chord spectrometer called DSS (Divertor Spectroscopy System) [34]. The blue dots indicate the locations of the Thomson Scattering measurements [35], and the cyan areas show the field-of-views of the two infrared cameras [36]. The right panel of figure 1 plots the 64 lines of sight of the gold foil bolometers, used to estimate the radiated power. The resulting line integrated chord intensities are tomographically inverted using a minimum Fisher regularization method [37]. Not shown on figure 1, but extensively used in this paper, are two different tangential optical cameras, MSI (*Multi-Spectral Imaging*) [38] and MANTIS (*Multispectral Advanced Narrowband Tokamak Imaging System*) [39, 40], used to gain further information on line radiations and distributions in the divertor region. These diagnostics have a polychromator layout where the same image is sequentially spectrally filtered and captured by a camera, with the remaining light reflected to the next filter. The captured images are inverted using the CalCam package [41, 42] to obtain two-dimensional poloidal maps of the emissivity of the selected radiation lines. In particular, in this paper, we will focus on NII (457.9 nm) and CIII (465.8 nm) line emissions, and determine the *un-calibrated* emissivity profiles. It should be noted that only one of these camera diagnostics is installed at a given time. Their measurement location is displaced toroidally from the operated gas valves by approximately 150° . A fast reciprocating probe, RCP [43, 44], is used to measure profiles of the electron temperature and density in the SOL at the outer midplane, once or twice per discharge. Its location is indicated by the orange rectangle in the left panel of figure 1.

In this work, we focus on a single-null configuration with a relatively large poloidal flux expansion of $f_x = 10$ at the outer strike-point. Such a configuration is drawn in both panels of figure 1. In TCV, this geometry leads to a significant drop of the outer target ion flux as the line-averaged density $\langle n_e \rangle$ is increased beyond a certain level [16, 42]. In sections 2 to 7, we explore detachment in this configuration in ohmic-heated discharges, with a relatively high plasma current $I_P \approx 340$ kA, permitting us to attain a high density regime. As in Ref. [16], the ∇B -drift is directed away from the X-Point. The paper focuses on the following three scenarios:

- (i) A $\langle n_e \rangle$ -ramp, where $\langle n_e \rangle$ is approximately linearly increased from $6 \times 10^{19} \text{ m}^{-3}$ (Greenwald fraction $f_G = 30\%$) to $12 \times 10^{19} \text{ m}^{-3}$ ($f_G = 60\%$).
- (ii) A “low”-density N_2 -seeding ramp, where the N_2 flux is linearly increased over time while $\langle n_e \rangle$ is kept approximately constant ($\approx 4.6 \times 10^{19} \text{ m}^{-3}$,

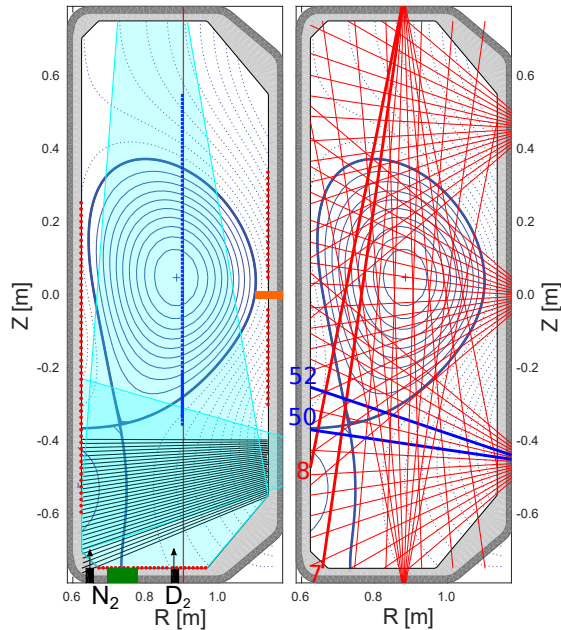


Figure 1. Typical geometry used in this article. The coverage of the main diagnostics used in this study is also indicated. In the left panel, the Langmuir probes (LPs) are indicated by red dots. The two cyan regions show the fields of view of the two infrared cameras, a vertical one and a horizontal one. The black rectangles at the bottom of the machine indicate the poloidal location of the gas valves used for fueling or seeding. The vertical red line is the interferometer chords used to evaluate the line-averaged density $\langle n_e \rangle$. The blue squares correspond to the measurements points of the Thomson Scattering (TS) system. The black lines correspond to the lines of sight of the Divertor Spectroscopy System (DSS). The orange rectangle indicates the location of the fast reciprocating probe (RCP). The green rectangle on the floor shows the port onto which the pressure gauge used to monitor divertor neutral pressure is attached via an extension tube. In the right panel, the different bolometry lines of sight are indicated. Four particular chords used in section 4 are highlighted: in red, chords 7 and 8, in blue, chords 50 and 52.

$$f_G \approx 23\%.$$

- (iii) A “high”-density N_2 -seeding ramp, where the N_2 flux is linearly increased over time while $\langle n_e \rangle$ is kept approximately constant ($\approx 9 \times 10^{19} \text{ m}^{-3}$, $f_G \approx 45\%$).

In both seeding cases, the N_2 seeding starts at $t = 0.8\text{s}$. The temporal evolution of the line-averaged density as well as the seeding and fueling fluxes for the different cases are summarized in figure 2. Also plotted in figure 2 are the evolution of the ohmic heating power P_{Ohm} , the core radiated power P_{rad}^{core} (estimated from the tomographic reconstruction of the bolometry signals) and $P_{SOL} = P_{Ohm} - P_{rad}^{core}$. We note that the “low”-density N_2 -seeding ramp disrupts at a later time (1.5s) than the other cases. This case further shows a

slight increase of $\langle n_e \rangle$ after 1.2s, coupled with a strong increase of the ohmic heating and P_{rad}^{core} , which could be explained by a penetration of N_2 inside the separatrix. This hypothesis is further supported by an increase of Z_{eff} inferred from an increase of the loop voltage V_{loop} . Using the expressions derived in Refs [45, 46], we find $Z_{eff} \approx 1.35$ before the introduction of N_2 in this discharge. Once the seeding starts at $t=0.8\text{s}$, Z_{eff} increases slightly up to $Z_{eff} \approx 1.6$ at $t=1.1\text{s}$. It then increases strongly, up to approximately $Z_{eff} \approx 3.5$ just before the discharge disrupts. In the high-density N_2 -seeding ramp, we observe no increase or possibly even a small decrease of $\langle n_e \rangle$ towards the end of the discharge, associated with only a weak increase of P_{rad}^{core} and a decrease of P_{SOL} . In this case, the increase of Z_{eff} remains modest, from about 1.3 before N_2 -seeding to about 1.45 when the discharge disrupts. While the behavior of the Z_{eff} could be attributed to a dilution effect, ongoing SOLPS-ITER simulations of these plasmas however confirm that the penetration of N_2 into the core is lower at high- $\langle n_e \rangle$. At high density, the core plasma thus appears to be better screened from N_2 injection into the divertor.

In section 8, where we investigate the effect of field direction, a different plasma scenario is used. While the geometry remains the same, the plasma current is reduced to $I_P \approx 245 \text{ kA}$ to avoid an Ohmic L-H transition in the favorable ∇B direction (ion ∇B -drift directed towards the X-Point). We examine four cases, divided into two scenarios, repeated with both field directions:

- (i) A $\langle n_e \rangle$ -ramp, where $\langle n_e \rangle$ is linearly increased from $4 \times 10^{19} \text{ m}^{-3}$ ($f_G \approx 25\%$) to $1 \times 10^{20} \text{ m}^{-3}$ ($f_G \approx 65\%$).
- (ii) A N_2 -seeding ramp, where the N_2 flux is linearly increased over time. N_2 seeding starts at $t = 0.8 \text{ s}$. Due to a poor stability of the density, $\langle n_e \rangle$ linearly increases from $3.5 \times 10^{19} \text{ m}^{-3}$ ($f_G \approx 22\%$) to approximately $4.5 \times 10^{19} \text{ m}^{-3}$ ($f_G \approx 30\%$).

A summary of the plasma discharges used in this work is presented in table 1, as well as the main quantities characterizing their scenarios.

3. Evolution of target quantities

3.1. Outer strike point

In figure 3, we plot the evolution of the total ion flux reaching the outer target, hereafter denoted Γ_t^o , as a function of time for the three cases described in section 2. In all cases, we observe a decrease of Γ_t^o at some point in time. In the $\langle n_e \rangle$ -ramp experiment, the roll-over occurs when a critical $\langle n_e \rangle$ ($\langle n_e \rangle \approx 1 \times 10^{20} \text{ m}^{-3}$) is reached, consistent with previous observations [16, 42]. However, it should be noted

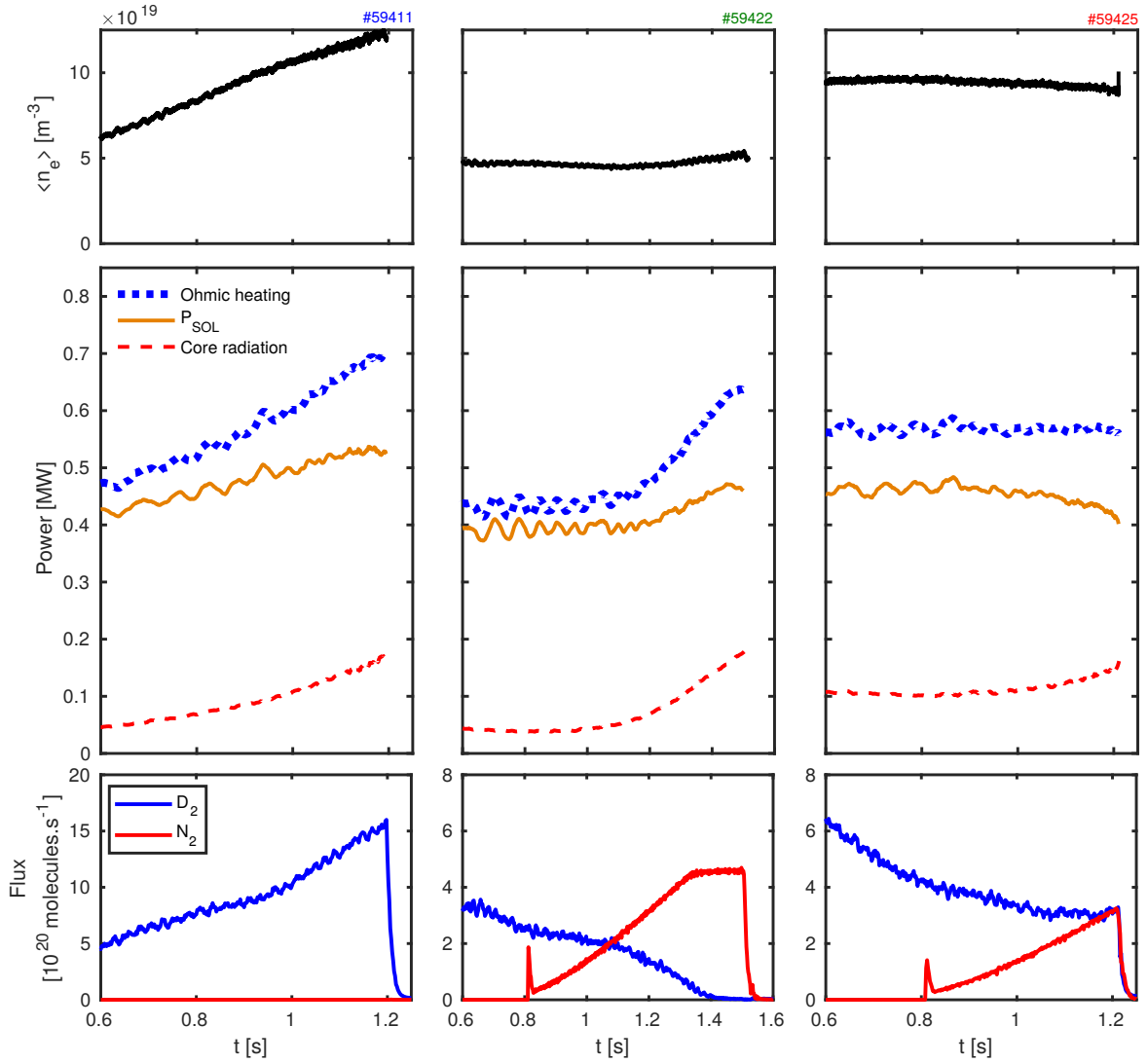


Figure 2. Time traces of the line-averaged density $\langle n_e \rangle$ (top), the evolution of the total ohmic heating, the core radiated power $P_{\text{rad}}^{\text{core}}$ (estimated from the bolometry reconstruction) and the power P_{SOL} going into the SOL (middle), and the evolution of the molecules fluxes (D_2 and N_2) for the different scenarios studied in this paper (bottom).

Discharge number	Density n_e	N_2 seeding	I_P	∇B direction
59411, 60417	Ramp	No N_2	340 kA	Unfavourable
59422	$\approx 4.6 \times 10^{19} \text{ m}^{-3}$	N_2 ramp	340 kA	Unfavourable
59425, 60015	$\approx 9 \times 10^{19} \text{ m}^{-3}$	N_2 ramp	340 kA	Unfavourable
57999	Ramp	No N_2	250 kA	Unfavourable
58001	Ramp	No N_2	250 kA	Favourable
61870	$3.5 \times 10^{19} \text{ m}^{-3} \rightarrow 4.6 \times 10^{19} \text{ m}^{-3}$	N_2 ramp	250 kA	Unfavourable
61872	$3.5 \times 10^{19} \text{ m}^{-3} \rightarrow 4.6 \times 10^{19} \text{ m}^{-3}$	N_2 ramp	250 kA	Favourable

Table 1. Summary of the main plasma discharges used in this work, with main parameters.

that in these previous discharges, higher core densities and thus a more pronounced roll-over was achieved, likely related to different wall conditions. Such a roll-over is generally considered as an indicator for the onset of detachment [12]. In the case of the N_2 -seeded discharges, a reduction of Γ_t^o is also observed. While

Γ_t^o starts to decrease as soon as N_2 is injected in the high-density N_2 -seeded scenario, for the low-density case, the reduction of Γ_t^o is observed ≈ 0.2 s after the start of seeding. This may be explained by the fact that the high-density case being close to detachment already before N_2 , thus requiring low seeding levels

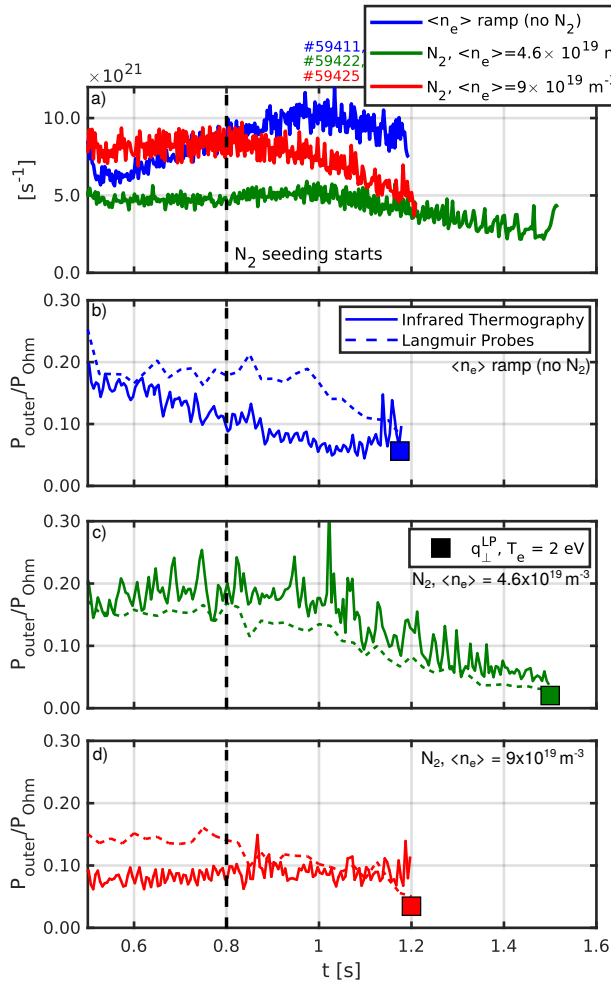


Figure 3. (top) Time evolution of the integrated outer target ion flux as a function of time for the three different cases discussed in this paper. The vertical dashed line indicates the start of the N_2 -seeding for the two cases where N_2 is injected. In each case, a reduction of the outer target ion flux is seen. (b, c, and d) Integrated power flux towards the outer target as measured by an infrared thermography system (solid lines) and deduced from the Langmuir probes measurements (dotted lines) for the different cases considered in this paper. We used equation 1, assuming $\gamma = 10$. The heat fluxes are normalized to the Ohmic power. The square markers indicate the heat flux measured by the Langmuir probes, computed using equation 1 and assuming a uniform target temperature $T_e = 2 \text{ eV}$.

before the onset of detachment. In panels b), c) and d) of figure 3, we plot the evolution of the integrated power reaching the outer target as a function of time for all cases, determined from an infrared thermography (IR) system (solid curve). In the $\langle n_e \rangle$ -ramp, and before the onset of detachment, we observe a continuous decrease of the power reaching the target as time (and therefore $\langle n_e \rangle$) is increased. However, after $t = 1.0 \text{ s}$, i.e. after the onset of detachment, we observe an increase of the power, contrary to expectations. This is also in contrast with the observed reduction of both the target ion flux and the target temperature

inferred by the Langmuir probes, and may result from surface reflections, bremsstrahlung emission [12, 47] or an inaccurate removal of the background radiation that invalidate the thermal analysis. In the case of N_2 -seeding, the situation appears even more complex. In the low-density case, a constant reduction of the power reaching the target is seen following the seeding, consistent with our expectations. In the high-density case, however, no such clear reduction of the power is seen from the infrared thermography measurement. Instead, the heat flux remains at a rather constant level ($\approx 50 \text{ kW}$). This observed behavior is reproducible, and this indicates that with our set-up, the use of the infrared thermography in detached conditions is not straightforward. To provide another estimate of the heat flux reaching the floor in detached conditions, we also plotted in panels b), c) and d) of figure 3 the heat flux evaluated from the Langmuir probes measurements (dashed curves). The heat flux perpendicular to the floor is evaluated as

$$q_{\perp} = j_{\text{sat}} (\gamma T_e + E_{\text{pot}}) \sin(\alpha) \quad (1)$$

where j_{sat} is the ion saturation current density along B , E_{pot} the potential energy carried by the incident ions ($E_{\text{pot}} = 13.6 + 2.2 = 15.8 \text{ eV}$, following Ref. [48]), γ the sheath heat transmission coefficient and α the grazing angle of the magnetic field with respect to the floor or target tiles. The heat flux is then integrated across the floor, assuming toroidal symmetry, leading to the dotted lines presented in figure 3. We have chosen $\gamma = 10$, which gives a fair agreement between the infrared measurements and the Langmuir ones in the low- $\langle n_e \rangle$, N_2 -seeded case, as well as in the low- $\langle n_e \rangle$ phase of the $\langle n_e \rangle$ -ramp. Furthermore, due to the difficulty to derive reliable T_e in detached regime (below 5 eV) with the probes (see ref. [32] and reference therein), we have also plotted the estimated target heat flux at the time of highest density/seeding level, assuming a uniform target temperature $T_e = 2 \text{ eV}$ (square markers).

From these LP measurements, we infer outer target heat flux reductions of up to 55% in the density ramp case (70% if $T_e = 2 \text{ eV}$ is assumed). For N_2 -seeding at low density, we read 80% (85%) and 65% (75%) for N_2 -seeding at high density. In previous density-ramp discharges [16], where higher core densities and a more pronounced roll-over were achieved, we find a reduction of the target heat flux of up to 89% (91% if $T_e = 2 \text{ eV}$ is assumed). Both density ramps and N_2 -seeding discharges reveal main features of outer target detachment - a significant drop in both heat and particle flux.

For more insight on the evolution of target profiles, we plot in figure 4 ion saturation current density j_{sat}^t , target electron density n_e^t , temperature T_e^t and target electron pressure p_e^t as measured by the LPs. In the left panels of figure 4 the profiles are measured

at $t = 0.75$ s, while in the right panels, the same quantities are shown immediately before the disruption that terminated the discharge. The radial coordinate ρ_ψ in these plots is the normalized poloidal magnetic flux, defined as $\rho_\psi = \sqrt{(\psi - \psi_0)/(\psi_1 - \psi_0)}$ where ψ is the poloidal magnetic flux with ψ_0 and ψ_1 the flux at the magnetic axis and at the primary X-point, respectively. In all cases, we clearly observe a reduction of the peak j_{sat} . A similar behavior is observed in the density profiles. As for the temperature profiles, a flattening can be observed in all three cases, with temperature dropping below 5 eV.

In the density ramp, the temperature profile obtained after detachment shows a high temperature peak near $\rho_\psi = 1$, leading to a similar peak on the pressure profile. As evidenced in Ref. [32], this is likely an artifact of the analysis. An Asymmetric Double Probe (ADP) fit [49, 32] suppresses this artificial peak near the strike point, as shown by the cyan curves in the right column of figure 4. We further note that the effect of impurity seeding on the density inferred by the LPs should remain limited, as shown in [50].

In all cases, the target pressure is reduced. In particular, the peak value of the target pressure decreased by a factor 2-3 in the density-ramp and at high-density with N_2 -seeding, while the reduction is even stronger at low-density with N_2 -seeding, where the peak is reduced by a factor ≈ 10 . In section 6, where we study the evolution of the upstream pressure, we will see that a pressure gradient indeed develops along the magnetic field in these cases, demonstrating the detached regime of the divertor.

3.2. Inner strike point

We now focus on the inner strike point. In Ref. [16], it was shown that, in the $\langle n_e \rangle$ -ramp experiments in TCV, the inner strike point does not appear to detach, which is in contrast to SOLPS-ITER [26] simulations of similar plasmas in the absence of drifts [51]. In the top panel of figure 5, we show the evolution of the integrated inner target ion flux Γ_t^i for all cases considered. The $\langle n_e \rangle$ -ramp does not exhibit a roll-over of Γ_t^i as $\langle n_e \rangle$ is increased, an indication of continued divertor attachment. We observe however a reduction of the rate at which Γ_t^i increases, a possible indication that it is approaching a roll-over (and hence the detachment) threshold. With N_2 -seeding, the situation changes. In both cases (low- and high-density), we observe a reduction of the target ion flux following the seeding. While the decrease of Γ_t^i is clear in the high-density case (a 50% reduction), it is less obvious at low-density. The lower panel of figure 5 plots the dynamics of the integrated power reaching the inner strike point inferred from infrared thermography. Unlike the outer strike point, the same tendency can be seen in all

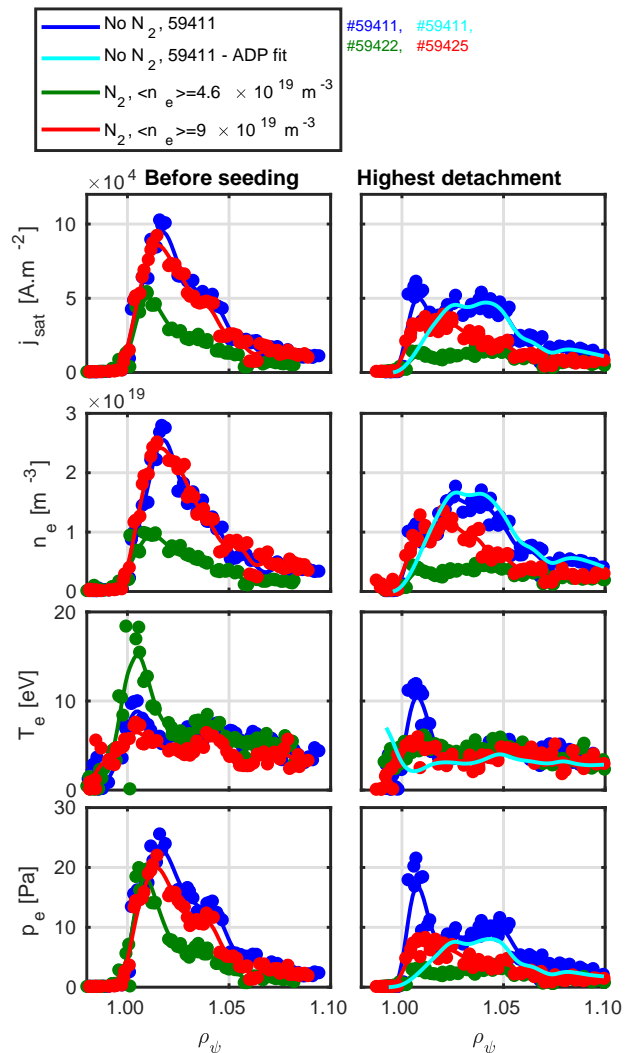


Figure 4. Outer target ion saturation current density j_{sat} , electron target density n_e^t , temperature T_e^t outer target electron pressure p_e^t profiles measured by the LPs. Left column: Profiles measured at $t=0.75$ s (before the N_2 -seeding starts) for the N_2 -seeded cases, and at $\langle n_e \rangle \approx 9 \times 10^{19} \text{ m}^{-3}$ for the density ramp case. Right column: Profiles measured just before the disruptions in the three different cases. The cyan profiles on the right plots correspond to quantities derived using another I-V fitting approach, the Asymmetric Double Probe Fit, described in [32].

three cases, that is, a progressive decrease of the power reaching the inner target. These results indicate that detachment of the inner strike point is achieved with N_2 -seeding, while in the $\langle n_e \rangle$ -ramp, we only approach the onset of detachment but do not achieve a reduction of the target ion flux.

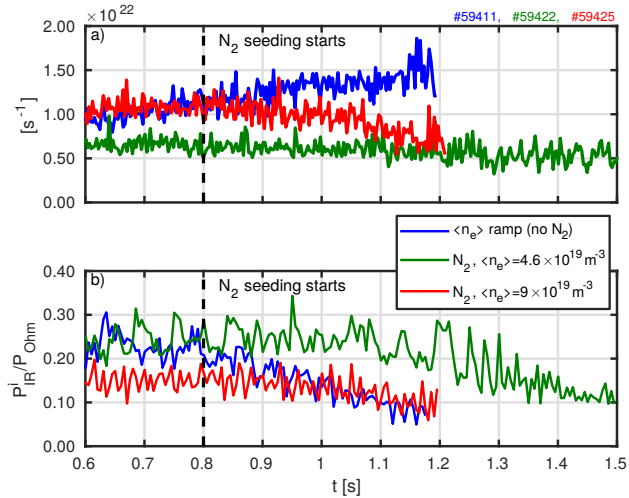


Figure 5. (top) Evolution of the integrated inner target ion flux as a function of time for the three different cases discussed in this paper. The vertical dashed line indicates the start of the N_2 -seeding for the two cases where N_2 is injected. (bottom) Integrated power flux towards the inner target as measured by an infrared thermography system for the different cases.

4. Power balance and radiation distribution

We now focus on the power balance and the spatial distribution of the radiation, as estimated by the bolometry. Figure 6 plots the SOL power ($P_{\text{SOL}} = P_{\text{Ohm}} - P_{\text{rad}}^{\text{core}}$) sharing between the targets (measured by the IR diagnostic for the inner one and the LP for the outer one), the radiation in the SOL, and the radiation around the X-Point. The definition of the core and X-Point region is indicated in cyan and red in the left panel of figure 6. In all cases, between 5% and 25% of the input power remains unaccounted, even after accounting for a systematic underestimation of the bolometry signal of approximately 15% [52], due to the reflection of some of the incident photons. An additional uncertainty in the present analysis is related to the accuracy of the tomographic reconstruction of the plasma emissivity. Such a reconstruction uncertainty is difficult to evaluate but is expected to be lower than the 15% uncertainty related to partial reflections on the bolometer foils. We then find that, initially, about 30% of the incoming power is radiated (in the SOL or near the X-Point) in the $\langle n_e \rangle$ -ramp, about 30% at low- $\langle n_e \rangle$ (without N_2 , yet), and around 60% at high- $\langle n_e \rangle$ (without N_2). As $\langle n_e \rangle$ is increased or N_2 puffed in the machine, all cases exhibit an increase in the radiated fraction while the power reaching both targets, P_{target} , decreases. At high-density, without N_2 , up to about 65% of P_{SOL} is radiated in the SOL and X-Point region. At high density with N_2 -seeding, about 80% of P_{SOL} is radiated, whereas at the low density with N_2 -seeding, about 60% of P_{SOL} is radiated. TCV being a carbon machine, we note that a

considerable fraction of the radiation likely comes from carbon impurities [18, 11].

The first four left columns of figure 7 plot the full emissivity profile, tomographically reconstructed from the bolometry signal. The outmost left column shows the emissivity profiles at $t=0.8$ s for all cases. For the $\langle n_e \rangle$ -ramp, three main radiation regions can be identified. Two are in the vicinity of the strike-points, and one near the X-Point. The low-density, N_2 -seeded case (although at $t=0.8$ s, N_2 has not been injected) shows a similar radiation structure. The high-density N_2 -seeded case, however, shows no radiation blob at the outer strike point. This indicates a proximity already to detachment. In the other columns, the emissivity is shown at later times. Overall, a similar behavior of radiation level and distribution is observed both for density ramps and N_2 seeding, with an increase in the radiation near the X-point and a decrease along the divertor leg. Total radiation levels, including the core, reach $\approx 80\%$. Some increase in core radiation is observed in all cases, although it is weak in the high- $\langle n_e \rangle$ seeding case. Ultimately, in all cases, the radiation strongly peaks around the X-Point, reminiscent of an X-Point radiator as observed in experiments in ASDEX-Upgrade [24, 53], or in previous TCV experiments with Neon-seeding [54]. Since the tomographic reconstruction of the bolometry data is subject to uncertainty, we further estimate the location of the radiation by using ratios of different bolometer chords. This is shown in the right column of figure 7, where the evolution of chords ratios are plotted for all three cases. The solid lines plot the evolution of the signal observed by chord 50 (as defined in figure 1) divided by the signal on chord 52. A decrease of this ratio indicates that the location of the radiation in the vicinity of the X-Point shifts above the X-Point. This is indeed what is observed in all three cases, hinting at the presence of a radiator region within the confined plasma. We also plot the ratio between chords 7 and 8 (see again figure 1 for definition). A decrease of this ratio indicates that the radiation region moves away from the ISP towards the X-point. This is found to happen in all cases. It should be noted that in the cases considered here, these X-Point radiators are not stable as we keep increasing either the fueling or the seeding rate. However, similar scenarios where $\langle n_e \rangle$ is kept at high value ($\approx 11.5 \times 10^{19} \text{ m}^{-3}$) show that such X-Point radiators can remain stable through the discharge, accounting for about 20% of the total radiated power. Although this value is lower than what is typically observed in H-Mode in JET or ASDEX-Upgrade ($\approx 40\%$ [24]), these experiments show that stable X-point radiator can also occur in carbon machines, at least in L-Mode.

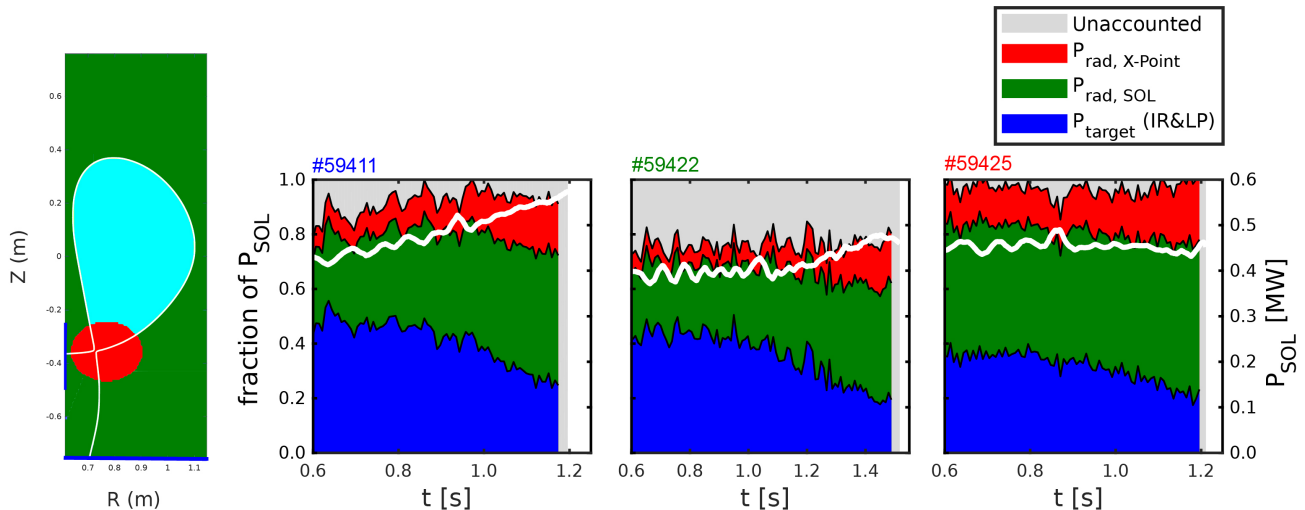


Figure 6. (left) Definition of the SOL region (green) and the X-Point region (red) and the core region (cyan). (right) Sharing of the power entering the SOL (P_{SOL}) between the targets (blue), the radiated power near the X-Point (red), and the radiated power in the rest of the SOL (green). The power reaching the target is computed using the infrared thermography measurements at the inner target, and the Langmuir probes measurement at the outer target (assuming $\gamma = 10$, see section 3). The gray areas correspond to the fraction of P_{SOL} that is unaccounted for when adding the radiated power to the infrared and Langmuir probe measured powers. It results from the uncertainties and limited coverage of the diagnostics, and varies here between 5% and 20%. (left) $\langle n_e \rangle$ -ramp, (center) N_2 -seeding ramp at $\langle n_e \rangle \approx 4.6 \times 10^{19} \text{ m}^{-3}$, (right) N_2 -seeding ramp at $\langle n_e \rangle \approx 9.0 \times 10^{19} \text{ m}^{-3}$. The white lines correspond to the absolute value of P_{SOL} (in MW), whose axis is located on the right of the figure.

5. Impurity front movement

In this section, we focus on the behavior of the impurity (carbon and nitrogen) radiation, and in particular on the CIII (465 nm) emissivity front location. As in previous studies [42, 16], we use it as a proxy for the location of the relatively cold ($\approx 3 - 8 \text{ eV}$) radiative region, useful to assess the proximity to detachment, the sensitivity of the cold front position on density or seeding level, or for detachment control [55]. However, in nitrogen seeded plasmas, the proximity of the NII lines (in the region ranging from 461 nm to 464 nm) to the CIII lines complicates the interpretation of the multi-spectra imaging data. Due to the spectral widths of the NII and the CIII filters installed on the cameras in these experiments, some NII lines will be picked-up by the CIII filter (and vice versa). Therefore, the resulting images are then a combination of CIII and NII radiations. This problem is discussed in more details in Ref. [29], which shows that mutual contamination of the two emissions are not substantially affecting the measurements.

In figure 8, the behavior of the CIII front movement is displayed for the three different cases. This front is determined as the location where the emissivity along the outer leg, estimated from tomographic inversion, has dropped by 50% [42]. All cases show a clear movement of the CIII front towards the X-Point. At high-density with N_2 -seeding, the front is initially already separated from the target. We also note that in all three cases, the movement of the

front is well correlated with the evolution of the (outer) target ion flux, plotted in figure 3, which motivates the use of the CIII front position along the divertor leg as a proxy to evaluate the detached state of the plasma in all these plasmas. Figure 8 also plots the behavior of the NII front movement. We observe a strong similarity to the CIII front behavior, which is not surprising since the radiative properties of nitrogen are similar to those of carbon. This proximity in the behavior could be used, for instance, to increase the robustness of control systems relying on the movement of an impurity to track the detached status of the divertor [56].

6. Evolution of upstream profiles and comparison to downstream profiles

After focusing mainly on the behavior at the target and in the divertor volume during density ramps and N_2 -seeding in the previous sections, we focus next on the evolution of the upstream quantities, which serve as “boundary conditions” for the core plasma. The separatrix quantities will be evaluated using the Thomson Scattering system and measurement from the fast reciprocating probe RCP. Due to the uncertainties in the magnetic equilibrium reconstruction, the ρ_ψ -mapping used to interpret the measurements appear to have a random uncertainty of several mm as discussed in Ref. [57]. To circumvent this issue, we shift the profiles so that the temperature at the separatrix matches the one computed using a method relying on

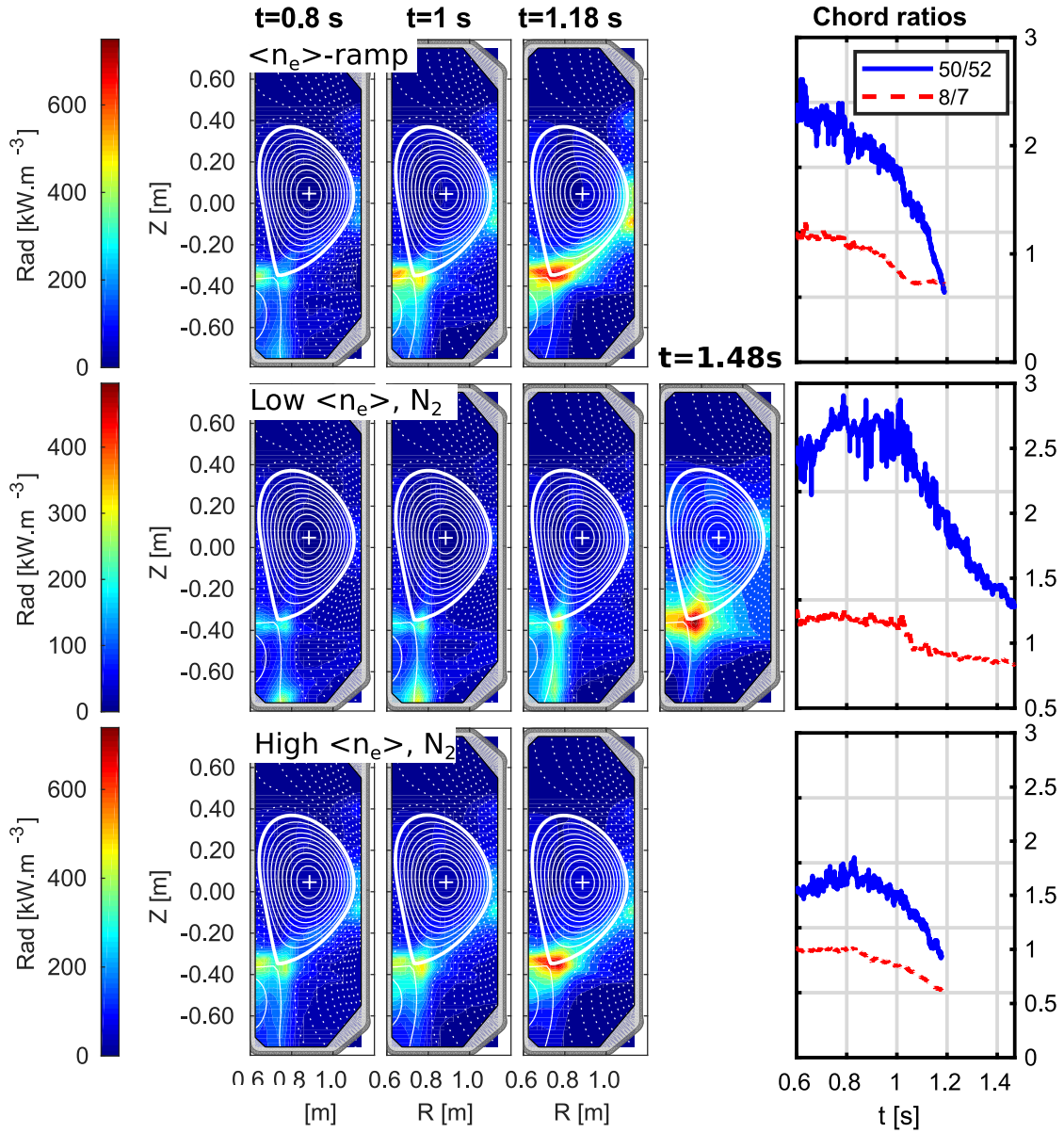


Figure 7. (first four columns) Tomographic reconstruction of the bolometry signals at given times for the three cases presented in this paper. $\langle n_e \rangle$ -ramp (top row), N_2 -seeding ramp at $\langle n_e \rangle \approx 4.6 \times 10^{19} \text{ m}^{-3}$, (middle row) N_2 -seeding ramp at $\langle n_e \rangle \approx 9.0 \times 10^{19} \text{ m}^{-3}$ (bottom row). Note that the color scales differ between the different rows. The last column shows the evolution of chord ratios. The chords used to plot these ratios are defined in figure 1.

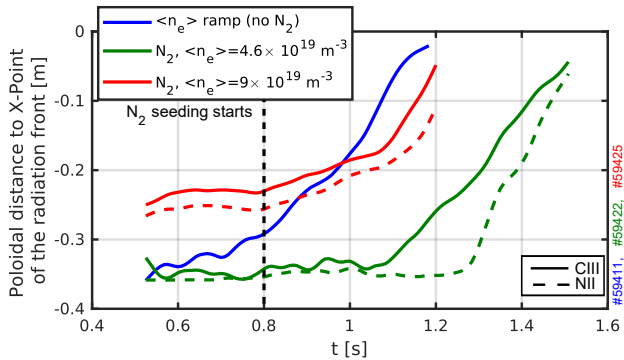


Figure 8. Poloidal distance between the CIII and NII fronts and the X-Point. The solid lines indicate the position of the CIII front, while the dashed lines indicate the position of the NII front, which is plotted only in case where N_2 is puffed in the machine.

power balance. This method, based on Refs. [58, 59], is discussed in detail in Appendix A. While this method has uncertainties of its own, they are systematic uncertainties. When using this method, we find that the pressure profile is more consistently balanced in low density conditions when comparing upstream and target conditions, as shown in the following section.

6.1. Evolution of upstream quantities

In figure 9, we plot the evolution of the upstream separatrix electron temperature T_e^{sep} , density n_e^{sep} and pressure p_e^{sep} in the $\langle n_e \rangle$ -ramp and the N_2 -seeded cases. The separatrix temperature and hence the separatrix position has been evaluated using equation A.9. In the N_2 -seeding cases, upstream quantities are found to be largely constant during the discharge. In the $\langle n_e \rangle$ -ramp instead, the rise of n_e^{sep} resulting from the increase of $\langle n_e \rangle$ results in a monotonic decrease of T_e^{sep} . The upstream pressure p_e^{sep} is seen to increase, which could be explained by the increase of the ohmic heating. In previous discharges, where higher $\langle n_e \rangle$ was reached, a roll-over of p_e^{sep} was observed [60, 11].

We find that in all cases, the separatrix density n_e^{sep} equals approximately $0.3 \times \langle n_e \rangle$, as shown in figure 9. In refs. [61, 62], it was found that the divertor neutral pressure p_n is the leading parameter in determining this quantity. In particular, it was found that $n_e^{sep} \propto p_n^{0.31}$ for AUG H-Mode seeded and unseeded discharges, while a scaling $n_e^{sep} \propto p_n^{0.5}$ was found based on a two-point model argument. Figure 10 plots the variation of the upstream electron density n_e^{sep} as a function of the divertor neutral pressure, measured by a baratron gauge installed on an extension tube connected to the floor of the machine (see figure 1). While an increase of n_e^{sep} with p_n is indeed observed in the density ramp, n_e^{sep} remains approximately constant during N_2 seeding. This discrepancy is currently not

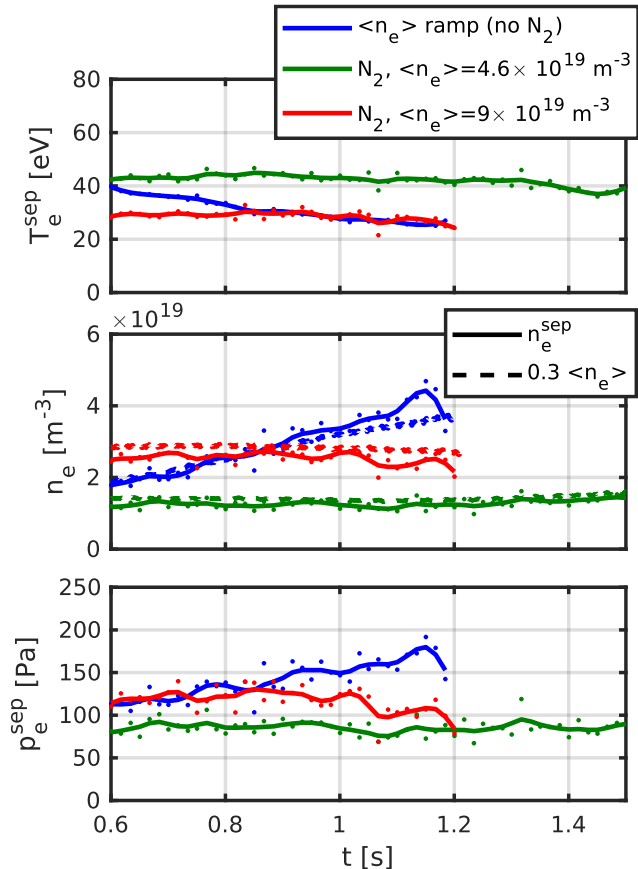


Figure 9. Evolution of upstream electron temperature T_e^{sep} (top), density n_e^{sep} (middle) and pressure p_e^{sep} as a function of time for the $\langle n_e \rangle$ -ramp and the N_2 -seeded cases. In the middle panel, $0.3 \times \langle n_e \rangle$ is also plotted in dashed lines. The points correspond to the values computed using equation A.9, while the solid lines correspond to fits of these data points.

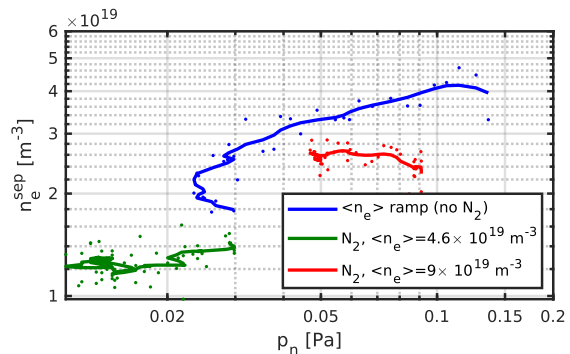


Figure 10. Evolution of the upstream electron density n_e^{sep} as a function of the divertor neutral pressure p_n for the $\langle n_e \rangle$ -ramp and the N_2 -seeded cases. The points correspond to the values computed using equation A.9, while the solid lines correspond to fits of these data points.

understood but may be related to the open TCV divertor.

Let us now compare the upstream and downstream pressure profiles, before and after the outer tar-

get ion flux drop in the different scenarios. In the fluid framework, from the momentum balance equation, one expects, in the absence of momentum losses and neglecting the variations of the magnetic field along the flux tube, and further assuming that $T_i = T_e$ [4]

$$n^u T_e^u \approx 2n^t T_e^t \quad (2)$$

where the superscript u (resp. t) indicates upstream (resp. target) location. To further quantify the drop between the upstream and target total pressures, we define f_{drop} as follows

$$f_{drop} = \frac{\int p_e^t d\rho}{\int p_e^u d\rho} \quad (3)$$

where the integration range for $\int p_e^t d\rho$ extends across the whole LP profile, and from $\rho = 1$ up to the furthest available point for $\int p_e^u d\rho$. It was checked that changing these ranges, for instance by taking a common range for the two integrals, does not impact the presented results. Using an integral definition for f_{drop} , instead of defining it for a particular ρ , allows alleviating possible effect of profiles misalignment or perpendicular momentum transport. In essence, f_{drop} is similar to the f_{mom} parameter introduced in the extended two-point model [4] and the integral momentum loss factor defined in [63]. In the following, we evaluate p_e^u using RCP, while p_e^t is measured by the floor Langmuir probes. Since the number of RCP plunges is limited to two within a single discharge, we performed a set of repeated, identical discharges where the RCP plunges at different times. In the case of the density ramp, this translates to plunges at different line-averaged densities. As for the N₂-seeding, the different plunges translate to different seeding rates. In all cases, the RCP profiles are then shifted using equation A.9, while the target profiles are not shifted. Figure 11 shows the evolution of f_{drop} for the $\langle n_e \rangle$ -ramp case (blue squares, top panel) and the N₂-seeding at high-density (blue squares, bottom panel). In both cases, a decrease of f_{drop} is observed, indicating that a parallel total pressure gradient between the outer midplane and the outer target has developed. f_{drop} drops to about 20% in the $\langle n_e \rangle$ -ramp, while for the N₂-seeding, it drops to about 40%. In the $\langle n_e \rangle$ -ramp case, the value is consistent with estimates of f_{mom} presented in Ref [11], where f_{mom} is evaluated using the Self-Ewald model [64, 11]. In figure 11, we also plotted the evolution of the (normalized) integrated ion flux to the outer target. In both cases, the target ion flux reduction coincides with the development of a parallel total pressure gradient. It therefore appears that the target ion flux evolution, which is experimentally easier to measure than f_{drop} , is a good proxy to assess the onset of a parallel pressure gradient, both in case of fueling and seeding. Finally, we note that while we used equation A.9 to shift the RCP

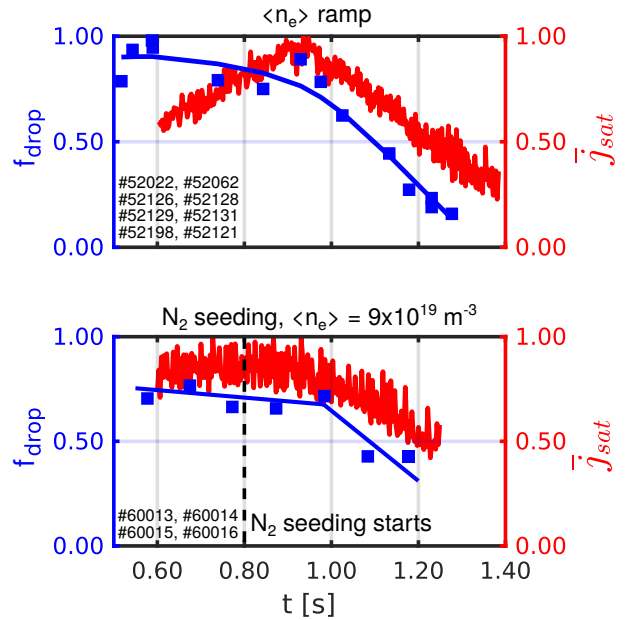


Figure 11. (blue squares and curves) Evolution of f_{drop} defined in equation 3 as a function of time in a $\langle n_e \rangle$ -ramp (top) and in a N₂-seeding case at high-density (bottom). In the bottom plot, the vertical dashed line indicates the start of the N₂-seeding. The evolution of the integrated ion flux to the outer target, normalized to its maximum value, is also plotted in red (associated to the right y-axis). In both cases, the development of a parallel pressure gradient represented by f_{drop} is well correlated with a reduction of the integrated ion flux to the outer target. The numbers in the lower left corners of the figures indicate the various discharges used to produce this plot.

profiles in figure 11, the observations and conclusions drawn from these remain the same if equation A.7 is used instead. We further note that in the absence of any profile shifting, we also observe a decrease of f_{drop} coincidentally with the roll-over of the outer target ion flux.

6.2. Observation of density shoulders

The observation of the upstream density profiles further reveals the onset of a density shoulder during $\langle n_e \rangle$ ramps in TCV, as discussed previously in [65, 42, 66, 67], as well as on other devices such as Alcator C-Mod [68, 69], Asdex-Upgrade [70, 71], DIII-D [72], JET [73] and JT-60U [74]. This shoulder formation is apparent in the middle panel of figure 12, showing a distinct broadening of the upstream density profile when increasing density and moving from attached to detached conditions. The top panel of figure 12 reveals that no such broadening is observed if detachment is instead accessed via N₂ seeding, as shown here for the high density seeding case. Focusing on the density ramp case in more detail, we show here that the onset of a density shoulder in the $\langle n_e \rangle$ -ramp case coincides with the roll-over of Γ_t^o , although a causality relation

between the two cannot be inferred. The top panel of figure 12 shows the evolution of the SOL density profile during this $\langle n_e \rangle$ -ramp. A broadening of the profiles is clearly visible as $\langle n_e \rangle$ is increased. In the bottom plot of figure 12, we quantify the evolution of the density profile width as a function of $\langle n_e \rangle$. To do so, we define a broadening parameter \tilde{n}_e as follows

$$\tilde{n}_e = \frac{1}{\Delta R} \frac{1}{n_e^{sep}} \int_0^{\Delta R} n_e dR \quad (4)$$

where $\Delta R = 3.5$ cm. In the case of a flat density profile ($n_e = n_e^{sep}$), $\tilde{n}_e = 1$, while for a very steep density profile, $\tilde{n}_e \rightarrow 0$. We note that other definitions exist for the amplitude of the shoulder, such as the one presented in Ref. [73]. The blue squares in the lower panel of figure 12 clearly show an increase of \tilde{n}_e as $\langle n_e \rangle$ is increased. Comparison with the target ion flux, also shown in the figure, reveals that the onset of the density shoulder coincides with the roll-over of the target ion flux. The shoulder formation then correlates with the negative slope in the target ion flux. Note that in figure 12, we do not shift the profile, unlike in section 6.1. For simplicity, we instead simply assume a possible 5 mm error, leading to error bars around the computed values of \tilde{n}_e . Again, in the nitrogen seeding case, also plotted in figure 12, no clear modification of \tilde{n}_e is seen as N_2 is injected. This indicates that the density shoulder formation is mainly affected by $\langle n_e \rangle$, and not by the divertor regime (attached/detached). Due to the broadening of the density profile, the shoulder could potentially modify the plasma-wall interaction at the outer-midplane, resulting for instance in a lower outer target ion flux after shoulder formation or enhanced power losses due to additional carbon erosion at the main wall.

7. Impact on confinement time

In this section, we explore the impact of accessing detachment on the stored energy and the confinement time. In the top panel of figure 13, we have plotted the stored energy W_{MHD} , deduced from a diamagnetic loop [75], for the different cases considered in this paper. In the density ramp case, we note a strong increase of W_{MHD} over time as $\langle n_e \rangle$ is increased, until $t = 1.0$ s, which coincides with the target ion flux rollover. Beyond this point, W_{MHD} starts to decrease, indicating a degradation of the confinement. In the low-density and high-density N_2 -seeded discharges, the stored energy slightly increases (despite approximately constant core conditions) before the decrease of target ion flux, and slightly drops afterwards. In the lower panel of figure 13, we have plotted the evolution of τ_E , the global energy confinement time, as a function of time for the different cases considered. We define τ_E

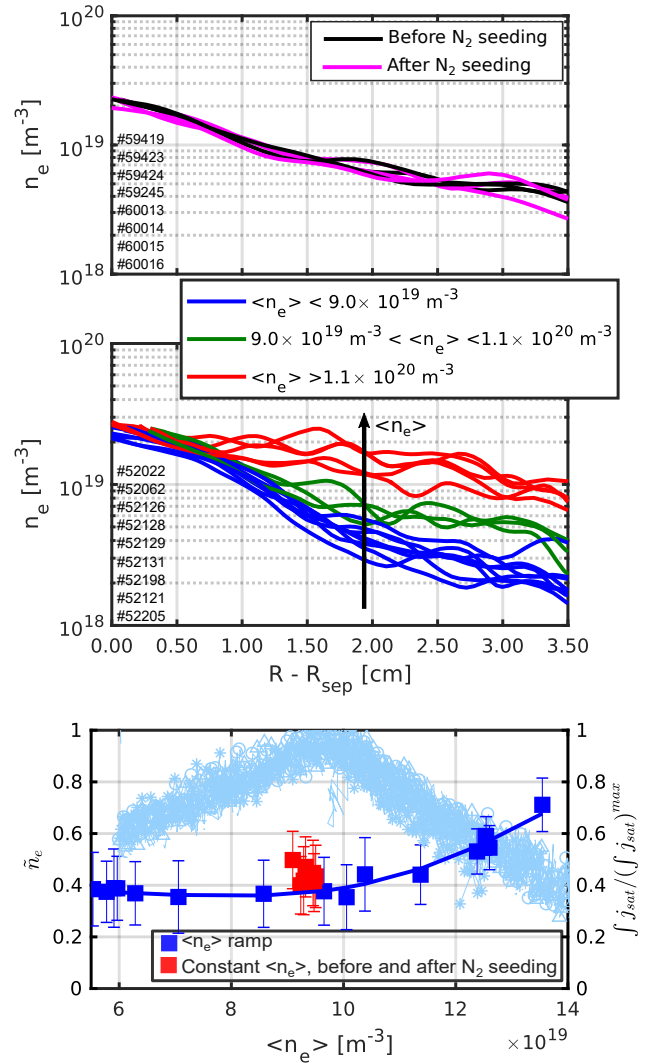


Figure 12. (top) Evolution of the outer midplane SOL density profile during a N_2 -seeding experiments at high- $\langle n_e \rangle$, before N_2 is introduced in the machine (black solid lines) and after (magenta solid lines). (middle) Evolution of the outer midplane SOL density profile during a $\langle n_e \rangle$ -ramp. The profiles are taken with the RCP [43, 44] at different times during well-reproducible discharges. The density profiles as a function of the distance to the separatrix. The color code indicates three different phases: (blue) $\langle n_e \rangle < 9.0 \times 10^{19} \text{ m}^{-3}$, (green) $9.0 \times 10^{19} \text{ m}^{-3} < \langle n_e \rangle < 1.1 \times 10^{20} \text{ m}^{-3}$ and (red) $\langle n_e \rangle > 1.1 \times 10^{20} \text{ m}^{-3}$. In the bottom plot, we show an estimate of the width of the profile using equation 4. The light blue curves indicate the normalized integrated ion flux to the outer target. The red points correspond to the width of the density profile evaluated for N_2 -seeded discharges, before and after N_2 is puffed. The numbers in the lower left corners of the top and middle panels indicate the various discharges used to produce this plot.

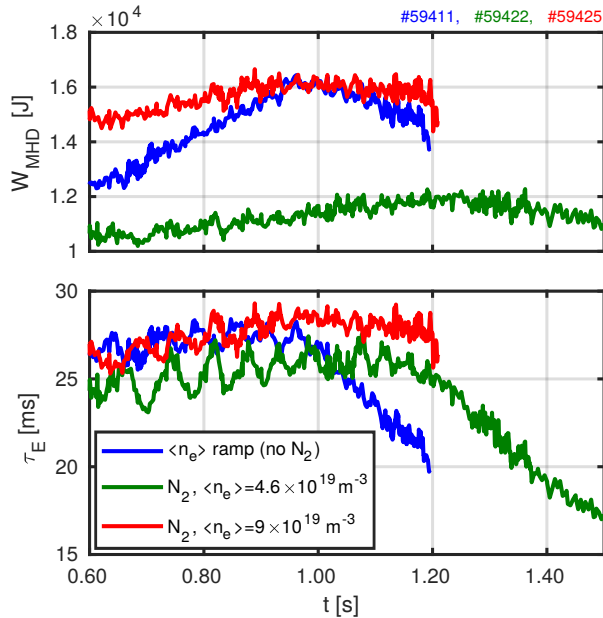


Figure 13. (top) Time evolution of W_{MHD} for the different cases considered in this paper. (bottom) Evolution of the global energy confinement time τ_E , defined in equation 5. We note that in all cases, the decrease of the target ion flux (as shown, for instance, in figure 3) appears to be well correlated with a decrease of τ_E .

as

$$\tau_E = \frac{W_{MHD}}{P_{in}} \quad (5)$$

where P_{in} the input power, which in the present cases is the ohmic power only. We note that in all cases, the decrease of the target ion flux (as shown, for instance, in figure 3) appears to be well correlated to a decrease of τ_E . However, the amplitude of the τ_E drop depends on the scenario. It is relatively large in the case of the $\langle n_e \rangle$ -ramp and the low-density, N_2 -seeded case, but remains marginal in the case of high-density, N_2 -seeded scenario, despite a large reduction of the outer target ion flux (as shown in figure 3). This smaller effect on τ_E at high-densities is consistent with lower levels of N_2 core penetration inferred in section 2. Thus, it is found that N_2 seeding provides a better compatibility with core confinement, but only if density is high enough to limit nitrogen influx into the core.

8. Influence of field direction

The cases discussed so far were performed in reversed field, which allowed us to operate at high current (340 kA) and thus high densities favorable for detachment, while avoiding transitions to H-mode. In view of H-mode detachment studies, which will mainly be performed in forward fields, we now explore the impact of field direction, and hence the direction of drifts,

on the observations made previously, in lower current plasmas ($I_P = 245$ kA) to avoid a transition to ohmic H-Mode in the forward field cases. The direction of the drifts is indeed known to significantly affect the behavior of the detachment onset, be it the detachment threshold or the dynamics of the transition to detachment [76, 10, 77]. It was for instance shown on DIII-D [78] that in H-Mode with the ∇B -drift oriented towards the X-Point, the detachment manifested itself as an abrupt bifurcation towards a cold divertor state.

N_2 -seeding and density ramp experiments have been performed both in “forward fields” (“favorable ∇B ” direction) and “reversed fields” (“unfavorable ∇B ” direction). Except for the lower I_P , these scenarios are similar to those in the previous chapters, including the geometry. In the N_2 -seeded experiment, the requested line-averaged density was approximately $4.6 \times 10^{19} \text{ m}^{-3}$. This was not very well achieved in the experiments, where the density slowly rises during the discharges from $3.5 \times 10^{19} \text{ m}^{-3}$ up to $4.75 \times 10^{19} \text{ m}^{-3}$, corresponding to a Greenwald fraction increase from 0.2 to about 0.3. However, since the discrepancy with the density reference was similar in both discharges (forward and reverse fields), a comparison remains meaningful. These discharges are compared to $\langle n_e \rangle$ -ramps in the same configuration, where the line-averaged density linearly increased from $3.5 \times 10^{19} \text{ m}^{-3}$ up to $8 \times 10^{19} \text{ m}^{-3}$ and no N_2 is injected.

8.1. Evolution of target quantities

In the top panel of figure 14, we have plotted the evolution of the outer target ion flux Γ_t^o in forward and reverse field cases, in both the $\langle n_e \rangle$ -ramp and N_2 -seeding experiments. Let us first discuss the $\langle n_e \rangle$ ramps. As time (and therefore $\langle n_e \rangle$) increases, a roll-over of Γ_t^o is seen in both field directions, at approximately similar times ($t \approx 1.4 - 1.5$ s), although in the forward-field case, a long “saturated” period can be seen before Γ_t^o starts to decrease. Furthermore, we observe that the roll-over in the reverse fields case is not a smooth decrease of Γ_t^o as seen in the higher current case (as plotted, for instance, in figure 3). It is rather a sudden drop of Γ_t^o . This behavior has been observed in several TCV discharges and seems to be typical in reverse-field with moderate I_P . We note also, in the forward field direction, the existence of large amplitude oscillations of Γ_t^o and Γ_t^i after the roll-over. These oscillations appear to be in phase between the two targets. Initially, those were suspected to be due to variations in the plasma shape. Indeed, the top triangularity in these discharges is quite high ($\delta_{top} \approx 0.35$), such that perturbations can lead to oscillations between a Lower-Single-Null (LSN) and a configuration closer to a Double-Null. However, a repetition of this discharge with a much

lower top triangularity ($\delta_{top} \approx 0.16$, #62356) also led to oscillations of the target ion flux (albeit of smaller amplitudes) and IR measurements. This could indicate the presence of oscillations in the detachment state, similar to those observed in JET [79] or ASDEX-Upgrade [10], even though we do not investigate further these observations here. As for the N_2 -seeding discharges, we observe a similar response of Γ_t^o in both forward and reverse-fields. Γ_t^o decreases as soon as N_2 is injected, although the decrease rate is somewhat higher in the forward field case.

More pronounced differences between forward and reversed fields are seen for the inner target ion flux Γ_t^i , as seen in the bottom panel of figure 14. In the $\langle n_e \rangle$ -ramps, Γ_t^i is seen to roll over for both field directions. However, the roll-over threshold is much lower in the forward field case, where, again, large scale oscillations are seen after 1.4 s. This indicates that detachment of the ISP is “easier” (i.e. at lower density) to achieve than in the reverse-field case, as known from other machines, such as JET [80]. In the N_2 -seeded experiments, Γ_t^i decreases right after the injection of N_2 in the forward fields case, whereas in the reverse fields, it only starts to clearly decrease 0.2 s after the injection of N_2 , and this decrease remains of modest amplitude.

In terms of absolute levels of particles flux, field direction shows a strong effect at the inner strike point, with substantially larger values in forward field. At the outer target, this effect is much weaker. These observations are consistent with previous TCV experiments and in parts with associated UEDGE simulations (including drift terms), where it was shown that changing the field direction in attached conditions affects the inner target more strongly than the outer one [81]. As in these simulations, the target density and temperature profiles at the ISP in our discharges show a higher density and a lower temperature in the forward field case than in the reverse field case. This is shown in figure 15, where we have plotted the target profiles of n_e and T_e determined by Langmuir probes at the inner strike point (ISP) and at the outer strike point (OSP) for reverse and forward field direction. All the profiles are plotted at the same line-averaged density $\langle n_e \rangle \approx 3.6 \times 10^{19} \text{ m}^{-3}$, in attached conditions. One can see that while the outer target profiles are relatively weakly affected by the change of field direction, a large difference can be seen at the ISP. While the pressure remains of similar order of magnitude (not shown), the density at the ISP is higher by a factor 2 in the forward field direction compared to the reverse field direction and the temperature is lower.

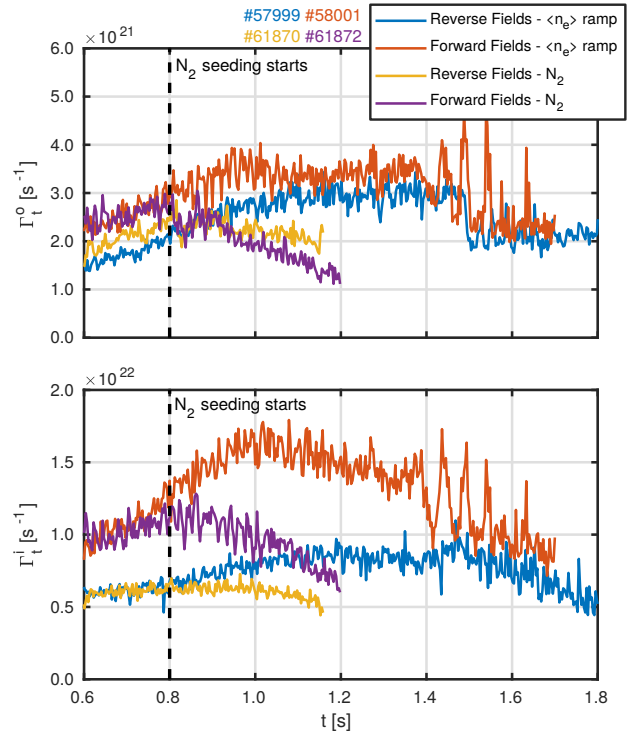


Figure 14. Dynamics of (top) outer target ion flux Γ_t^o (bottom) inner target ion flux Γ_t^i in forward and reverse field cases, in $\langle n_e \rangle$ -ramp and N_2 -seeding experiments.

A similar trend can be observed after detachment, with the density at the ISP still being higher in the forward field direction than in the reverse field direction (not shown).

Recent detachment modeling of TCV reverse-field plasmas with SOLPS have generally revealed a better agreement with experiments at the outer target as compared to the inner one [82, 11]. These simulations did not include drifts. Our observations presented here (that field direction primarily affects the inner target) indicate that drifts could be the main missing element for a better match with simulations. They were for instance shown to be critical in matching experiment observations in ASDEX-Upgrade [83, 84], Alcator C-Mod [85] and JET [84].

8.2. Impact of field direction on radiation distribution

Due to the different orientation of the fields and hence of the drifts, one can expect a different radiation distribution pattern between forward and reverse fields. This is indeed the case, as shown in figure 15, where the two-dimensional emissivity maps, computed from bolometric measurements, are plotted at different times for both field directions and different N_2 seeding levels. We observe that in the reverse field case, two radiation blobs can be seen, one near the X-point and the other one near the inner strike-point.

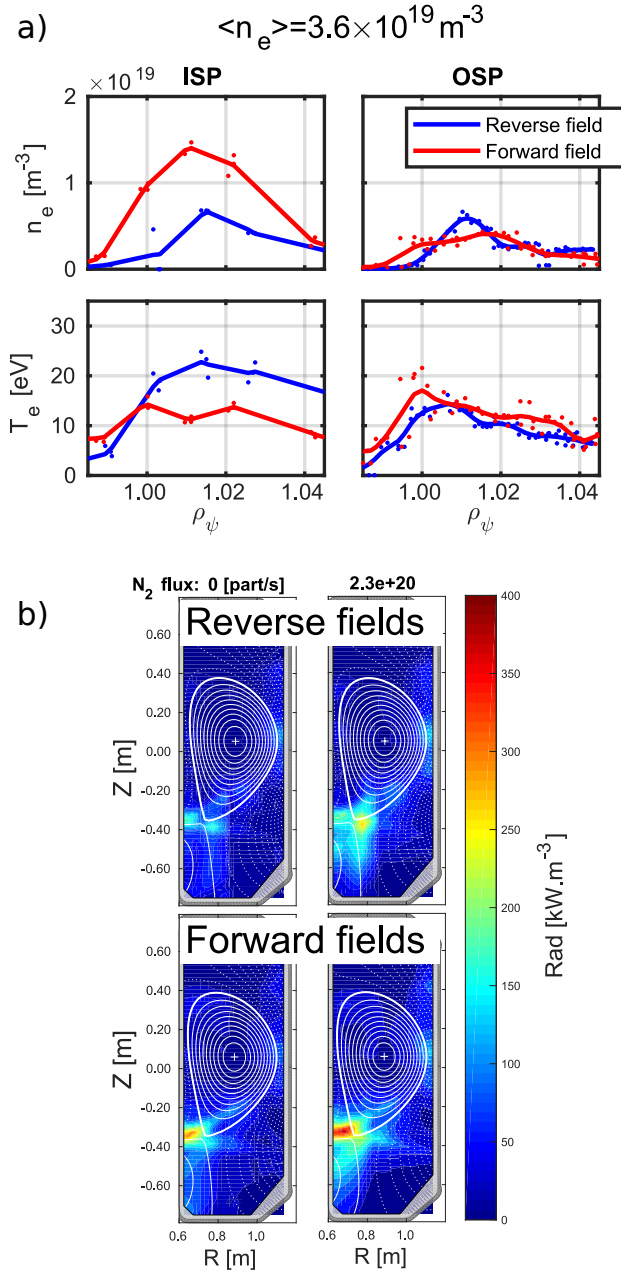


Figure 15. a) Target profiles of n_e (top) and T_e (bottom) determined by Langmuir probes at the inner strike point (ISP) (left) and at the outer strike point (OSP) (right) for reverse field (blue) and forward field (red). All the profiles are plotted at the same line-averaged density $\langle n_e \rangle = 3.6 \times 10^{19} \text{ m}^{-3}$ ($f_G \approx 0.25$), where the plasma is attached b) Radiation distribution in presence of N_2 -seeding in (top line) reverse fields and (bottom line) forward fields. The color scale is common to all the plots..

As more N_2 is injected, the radiation concentrates around the X-point. In the forward field case, only one radiation blob can be seen, between the inner strike-point and the X-point. Its amplitude is substantially higher (approximately $2\times$) than the levels observed in reversed field. This increased level of radiation could originate from the higher density measured at the inner target in the forward-field case. This observation is compatible with observations on other devices [86], where strong radiation at the inner strike point are seen in the forward field direction.

A crude interpretation can be made using the total loss power function L_z (see Ref. [8] and references therein), defined such that the local emissivity ϵ_{imp} from an impurity of concentration c_{imp} is given by $\epsilon_{imp} = c_{imp} n_e^2 L_z$. In the range of n_e measured near the divertor targets, and assuming constant pressure $p_e = n_e T_e = 25 \text{ Pa}$, computation of ϵ_{imp} shows that increasing n_e indeed leads to an increase of the radiation, even though the temperature decreases. This is consistent with the observation reported in figures 15, where higher radiation near the ISP are observed in forward field, associated with higher density and lower temperature. The higher radiation levels and lower T_e at the ISP in forward field are therefore likely the reason for the easier detachment of the ISP in such field direction. We insist however on the fact that this remains only a crude interpretation, which largely ignores the effect of transport, which has a tremendous impact on the radiative properties of the different species.

9. Summary and conclusion

In this paper, we presented the main observations of the N_2 detachment experiments in TCV LSN L-Mode plasmas. At both low- and high- $\langle n_e \rangle$, a drop of the ion flux and heat flux to the inner and outer strike-points is observed after the injection of N_2 , whereas in $\langle n_e \rangle$ -ramp, only the outer strike-point appears to detach. The low temperature measured at the outer strike-point, as well as the onset of a pressure drop between the outer mid-plane and the outer target, confirm the detached nature of the outer divertor in all cases. In the density ramp, a degradation of the confinement time τ_E is observed at the onset of detachment, whereas in the N_2 -seeding experiments, the confinement time is affected only at later times. In these cases, confinement degradation likely occurs because of the penetration of nitrogen into the core, as evidenced by the increased radiated power in the core, as well as the increase of Z_{eff} inferred from the increase of the loop voltage V_{loop} . In the N_2 -seeding case at high- $\langle n_e \rangle$, the degradation of τ_E remains, however, small, which makes this a promising scenario

for divertor-core compatibility. Radiation levels of up to approximately 80% of the Scrape-Off Layer (SOL) input power are achieved and outer target heat fluxes are reduced by up to 90% compared to attached conditions. Depending on the plasma density, the location of the radiation changes. At low density, the radiation in the outer leg peaks close to the target. As density is increased or N₂ seeded, instead, a radiation peak around the X-Point forms, which accounts for ≈20% of the total radiated power and is reminiscent of X-Point radiators on AUG and JET. For both seeding and fueling, the observation of the CIII emission shows a “front” receding from the target towards the X-Point, this movement being well correlated with the evolution of the target ion flux. This confirms the good experimental proxy that constitutes the monitoring of the CIII front location for detachment evolution on TCV. Measurements of the upstream and target pressure profiles reveal that the I_{sat} roll-over and the parallel pressure drop occur simultaneously, both for the $\langle n_e \rangle$ -ramp and N₂-seeding at high density, showing that the roll-over of the target ion flux is indeed a good indicator for the detachment onset. During the $\langle n_e \rangle$ -ramp, we further observe that the roll-over of the outer target ion flux coincides with the broadening of the upstream density profile, which forms a “shoulder”. No such broadening is seen in N₂-seeding experiments, where the upstream quantities (temperature, density) also remain approximately constant. The impact of the ∇B -drift direction on the detachment properties has also been explored. For both density ramps and nitrogen seeding, field direction is found to mainly affect the behavior of the inner strikepoint, with an easier detachment in forward fields. This seems to be associated with higher densities and lower temperature at the ISP in forward field as compared to reverse field, as well as increased levels of radiation near the ISP. As shown in Ref. [81], the $E \times B$ -drift can explain the higher density and lower temperature observed at the ISP in forward field. The higher radiation level is expected for an increase in density, when pressure and impurity content are unchanged. These experiments therefore show that the inclusion of drifts is of paramount importance to reproduce correctly the behavior of the inner strike point in simulations.

The detailed analysis and diagnostics interpretation of nitrogen seeded TCV detachment experiments presented in this work will provide a basis for ongoing studies in H-Mode and alternative geometries and associated modeling.

Acknowledgments

This work was supported in part by the Swiss National Science Foundation. This work was supported by

the U.S. Department of Energy under Grant No. DE-SC0010529. This work has been carried out within the framework of the EUROfusion Consortium and has received funding from the Euratom research and training programme 2014 - 2018 and 2019 - 2020 under grant agreement No 633053. The views and opinions expressed herein do not necessarily reflect those of the European Commission.

Appendix A. Estimate of separatrix quantities

Due to uncertainties in the LIUQE equilibrium reconstruction, the ρ_ψ -mapping and in particular the determination of the separatrix position ($\rho_\psi = 1$) is subject to uncertainties. In this section, we use the two-point model predictions coupled to a power balance argument to estimate the upstream separatrix temperature. Combined with a measurement of the upstream SOL temperature profile, e.g. from Thomson Scattering or fast reciprocating probe diagnostics, this then provides an estimate of the separatrix position. The method that we use is based on Refs. [58, 59].

From power balance, the peak value of the upstream parallel electron heat flux, $q_{e,\parallel}^{peak}$, can be estimated as

$$q_{e,\parallel}^{peak} = \frac{1}{2\pi R_{sep}} \frac{f P_e^{tar} B_{tot}}{\lambda_q B_{pol}} \quad (\text{A.1})$$

where R_{sep} is the radial position of the separatrix, λ_q the characteristic decay length of the parallel heat flux and $\frac{B_{tot}}{B_{pol}}$ the ratio of the total magnetic field to the poloidal magnetic field. These three quantities are all defined at the outer midplane. P_e^{tar} is the power entering the SOL and being carried towards both targets by the electrons, and f the fraction of this power that goes into the outer leg. Evaluation of equation A.1 requires in particular the knowledge of λ_q . In this study, we infer λ_q from IR thermography. The target heat flux profile is mapped to the upstream location, and the Eich fit is then applied to determine λ_q . It is observed in this set of discharges that λ_q depends on $\langle n_e \rangle$ as shown in figure A1. We find that λ_q is well fitted by a second-order polynomial

$$\lambda_q = a \langle n_e \rangle^2 + b \quad (\text{A.2})$$

with $a = 7.934 \times 10^{-43} \text{ m}^7$, $b = 6.891 \times 10^{-4} \text{ m}$. The values of λ_q that we estimated here in well-attached plasmas (ie at low- $\langle n_e \rangle$, without N₂) are compatible with the values presented in Ref. [36]. To evaluate λ_q for $\langle n_e \rangle$ higher than 10^{20} m^{-3} , we extrapolate the values using equation A.2. Assuming that the electron heat flux is carried from the outer midplane towards the outer target only by conduction following the Spitzer-Härm thermal conductivity, one can write

$$q_{e,\parallel} = -\kappa_e^0 T_e^{5/2} \frac{\partial T_e}{\partial s} = -\frac{2}{7} \kappa_e^0 \frac{\partial T_e^{7/2}}{\partial s} \quad (\text{A.3})$$

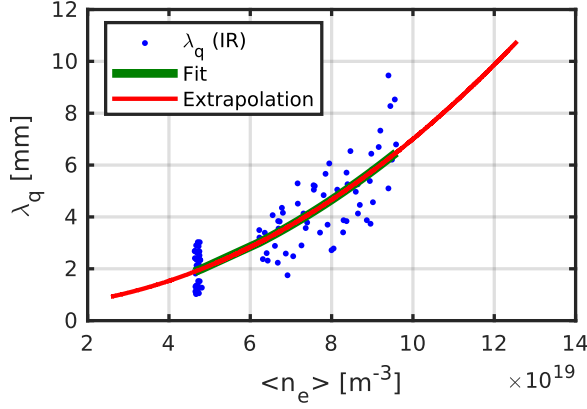


Figure A1. λ_q inferred from IR thermography. The green curve corresponds to a fit of all the IR data points, given by equation A.2. The red curve presents the extrapolation of this fit to higher densities.

where $\kappa_e^0 \approx 2300 \text{ W.m}^{-1}.\text{eV}^{-\frac{7}{2}}$ is the Spitzer-Härm heat conductivity coefficient for the electrons and s is a curvilinear coordinate along a field line. We now evaluate equation A.3 at the separatrix location. Neglecting the changes of the magnetic field along the flux tube and assuming $q_{e,\parallel}$ constant along B (no volumetric power losses or cross-field transport), one can integrate equation A.3 to find:

$$q_{e,\parallel}^{peak} = \frac{2}{7} \kappa_e^0 \frac{\left((T_e^{sep})^{7/2} - (T_e^t)^{7/2} \right)}{L_{\parallel}} \quad (\text{A.4})$$

where T_e^{sep} is the electron temperature at the upstream separatrix, T_e^t is the electron temperature at the target and L_{\parallel} the parallel connection length. Equating this expression with equation A.1, we obtain

$$\frac{2}{7} \kappa_e^0 \frac{\left((T_e^{sep})^{7/2} - (T_e^t)^{7/2} \right)}{L_{\parallel}} = \frac{1}{2\pi R_{sep}} \frac{f P_e^{tar}}{\lambda_q} \frac{B_{tot}}{B_{pol}} \quad (\text{A.5})$$

leading to

$$T_e^{sep} = \left(T_e^t{}^{7/2} + \left[\frac{7}{2\kappa_e^0} \frac{L_{\parallel}}{2\pi R_{sep}} \frac{f P_e^{tar}}{\lambda_q} \frac{B_{tot}}{B_{pol}} \right]^{2/7} \right)^{2/7} \quad (\text{A.6})$$

To evaluate equation A.6, we now need to estimate P_e^{tar} , the power going to the target that is carried by the electrons. We assume that the electrons carry half of the total power reaching the target, P_e^{tar} , such that $P_e^{tar} = 0.5 P^{tar}$. This assumption implies that $T_i > T_e$ in the SOL, which is consistent with the charge-exchange data for these shots (not shown here) and with the value used in [59]. As for the value of P_e^{tar} , we explore two possible assumptions:

(i) No power is radiated in the SOL, so that the total power entering the SOL is transported towards the

targets. Therefore, $P_e^{tar} = P_{SOL}$. Equation A.6 can then be rewritten as

$$T_e^{sep} = \left((T_e^t)^{7/2} + \left[\frac{7}{2\kappa_e^0} \frac{L_{\parallel}}{4\pi R_{sep}} \frac{f (P_{Ohm} - P_{rad}^{core})}{\lambda_q} \frac{B_{tot}}{B_{pol}} \right]^{2/7} \right)^{2/7} \quad (\text{A.7})$$

Within our model, this case is equivalent to assuming that there is power being radiated in the SOL, but that all of this radiation occurs just in front of the target plates.

(ii) All the power radiated in the SOL is assumed to be radiated at the outer midplane, and therefore the total power actually flowing to the target is

$$P_e^{tar} = P_{SOL} - P_{rad}^{SOL} \quad (\text{A.8})$$

where P_{rad}^{SOL} is the power radiated in the SOL, measured by the bolometry. It is further assumed that the radiated power is equally lost between the ion and electrons. Following a similar reasoning as for equation A.7, one then gets

$$T_e^{sep} = \left((T_e^t)^{7/2} + \left[\frac{7}{2\kappa_e^0} \frac{L_{\parallel}}{4\pi R_{sep}} \frac{f (P_{Ohm} - P_{rad}^{tot})}{\lambda_q} \frac{B_{tot}}{B_{pol}} \right]^{2/7} \right)^{2/7} \quad (\text{A.9})$$

where $P_{rad}^{tot} = P_{rad}^{SOL} + P_{rad}^{core}$

These two equations (A.7 and A.9) provide a quantitative estimate of the separatrix temperature depending on the plasma magnetic configuration (L_{\parallel} , R_{sep} , B_{tot} and B_{pol}), power into the SOL (P_{SOL}) and transport properties (f , λ_q). Possible errors on the evaluation of these parameters will be attenuated by the $2/7$ exponent, leading, in principle, to a robust estimate of T_e^{sep} . In figure A2, we have plotted the evolution of the upstream separatrix temperature as predicted by equations A.7 and A.9, and compare it to the measurements provided by the Thomson Scattering system, assuming accurate knowledge of the separatrix location from the equilibrium reconstruction. To do so, we assumed $T_e^t \approx 0$, which can be neglected within our conduction-limited model if [4]

$$\nu^* \approx 10^{-16} \frac{n_e^{sep} L_{\parallel}}{T_e^{sep2}} \geq 15 \quad (\text{A.10})$$

where n_e^{sep} is the upstream separatrix electron density. In our case, we find this criterion to be well satisfied during the $\langle n_e \rangle$ -ramp and the high-density N_2 -seeding discharges. In the low density N_2 -seeded discharge, we find that $\nu^* \approx 10 - 15$ and the criterion is only marginally satisfied. Overall, a satisfactory agreement with the Thomson Scattering is found, even so it appears that the Two-Point Model method tends to yield slightly higher temperatures than the un-shifted TS measurements, which could indicate that the magnetic equilibrium reconstruction tends to position the separatrix too far out. The top panel of figure A2 also plots equation A.7 evaluated with a constant $\lambda_q = 5 \text{ mm}$. This results in a different trend in upstream temperature, highlighting the need to account for the dependence of λ_q on $\langle n_e \rangle$.

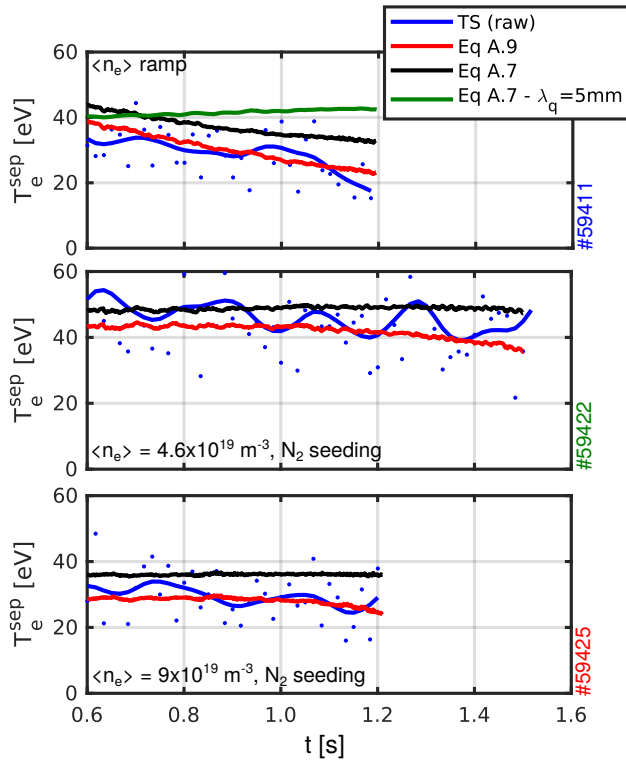


Figure A2. Upstream temperature determined from equations (black) A.7 and (red) A.9 for the different discharges studied in this paper. The dashed blue line indicates the temperature obtained with the un-shifted TS measurements. Overall, a satisfactory agreement with the Thomson Scattering is found, even so it appears that the Two-Point Model method tends to yield slightly higher temperatures than the un-shifted TS measurements. In the top panel, we also plot in green equation A.7 evaluated with a constant $\lambda_q = 5$ mm.

References

- [1] Loarte A, Lipschultz B, Kukushkin A, Matthews G, Stangeby P, Asakura N, Counsell G, Federici G, Kallenbach A, Krieger K, Mahdavi A, Philipps V, Reiter D, Roth J, Strachan J, Whyte D, Doerner R, Eich T, Fundamenski W, Herrmann A, Fenstermacher M, Ghendrih P, Groth M, Kirschner A, Konoshima S, LaBombard B, Lang P, Leonard A, Monier-Garbet P, Neu R, Pacher H, Pegourie B, Pitts R, Takamura S, Terry J, Tsitrone E, the ITPA Scrape-off Layer and Group D P T 2007 *Nuclear Fusion* **47** S203
- [2] Pitts R, Bardin S, Bazylev B, van den Berg M, Bunting P, Carpentier-Chouchana S, Coenen J, Corre Y, Dejarnac R, Escourbiac F, Gaspar J, Gunn J, Hirai T, Hong S H, Horacek J, Iglesias D, Komm M, Krieger K, Lasnier C, Matthews G, Morgan T, Panayotis S, Pestchanyi S, Podolnik A, Nygren R, Rudakov D, Temmerman G D, Vondracek P and Watkins J 2017 *Nuclear Materials and Energy* **12** 60 – 74 ISSN 2352-1791 proceedings of the 22nd International Conference on Plasma Surface Interactions 2016, 22nd PSI
- [3] Wischmeier M 2015 *Journal of Nuclear Materials* **463** 22 – 29 ISSN 0022-3115 plasma-Surface Interactions 21
- [4] Stangeby P 2000 *The Plasma Boundary of Magnetic Fusion Devices* Series in Plasma Physics and Fluid Dynamics (Taylor & Francis) ISBN 9780750305594

- [5] Krasheninnikov S I, Kukushkin A S and Pshenov A A 2016 *Physics of Plasmas* **23** 055602
- [6] Leonard A W 2018 *Plasma Physics and Controlled Fusion* **60** 044001
- [7] Stangeby P and Leonard A 2011 *Nuclear Fusion* **51** 063001
- [8] Kallenbach A, Bernert M, Dux R, Casali L, Eich T, Giannone L, Herrmann A, McDermott R, Mlynek A, Müller H W, Reimold F, Schweinzer J, Sertoli M, Tardini G, Treutterer W, Viezzer E, Wenninger R, Wischmeier M and the ASDEX Upgrade Team 2013 *Plasma Physics and Controlled Fusion* **55** 124041
- [9] Lipschultz B, LaBombard B, Terry J L, Boswell C and Hutchinson I H 2007 *Fusion Science and Technology* **51** 369–389
- [10] Potzel S, Wischmeier M, Bernert M, Dux R, Müller H, Scarabosio A and the ASDEX Upgrade Team 2014 *Nuclear Fusion* **54** 013001
- [11] Verhaegh K, Lipschultz B, Duval B, Février O, Fil A, Theiler C, Wensing M, Bowman C, Gahle D, Harrison J, Labit B, Marini C, Maurizio R, de Oliveira H, Reimerdes H, Sheikh U, Tsui C, Vianello N, Vijvers W and and 2019 *Nuclear Fusion* **59** 126038
- [12] Loarte A, Monk R, Martín-Solís J, Campbell D, Chankin A, Clement S, Davies S, Ehrenberg J, Erents S, Guo H, Harbour P, Horton L, Ingesson L, Jäckel H, Lingertat J, Lowry C, Maggi C, Matthews G, McCormick K, O'Brien D, Reichle R, Saibene G, Smith R, Stamp M, Stork D and Vlases G 1998 *Nuclear Fusion* **38** 331
- [13] Lipschultz B, Goetz J, LaBombard B, McCracken G, Terry J, Graf M, Granetz R, Jablonski D, Kurz C, Niemczewski A and Snipes J 1995 *Journal of Nuclear Materials* **220-222** 50 – 61 ISSN 0022-3115 plasma-Surface Interactions in Controlled Fusion Devices
- [14] Petrie T, Hill D, Allen S, Brooks N, Buchenauer D, Cuthbertson J, Evans T, Ghendrih P, Lasnier C, Leonard A, Maingi R, Porter G, Whyte D, Groebner R, Jong R, Mahdavi M, Thompson S, West W and Wood R 1997 *Nuclear Fusion* **37** 321–338
- [15] Hosogane N, Asakura N, Kubo H, Itami K, Sakasai A, Shimizu K, Nakamura H, Shimada M, Neyatani Y and Yoshino R 1992 *Journal of Nuclear Materials* **196-198** 750 – 754 ISSN 0022-3115 plasma-Surface Interactions in Controlled Fusion Devices
- [16] Theiler C, Lipschultz B, Harrison J, Labit B, Reimerdes H, Tsui C, Vijvers W A J, Boedo J A, Duval B P, Elmore S, Innocente P, Kruezi U, Lunt T, Maurizio R, Nespoli F, Sheikh U, Thornton A J, van Limpt S H M, Verhaegh K, Vianello N, the TCV team and the EUROfusion MST1 team 2017 *Nuclear Fusion* **57** 072008
- [17] Reimerdes H, Duval B, Harrison J, Labit B, Lipschultz B, Lunt T, Theiler C, Tsui C, Verhaegh K, Vijvers W, Boedo J, Calabro G, Crisanti F, Innocente P, Maurizio R, Pericoli V, Sheikh U, Spolare M, Vianello N and and 2017 *Nuclear Fusion* **57** 126007
- [18] Fenstermacher M E, Boedo J, Isler R C, Leonard A W, Porter G D, Whyte D G, Wood R D, Allen S L, Brooks N H, Colchin R, Evans T E, Hill D N, Lasnier C J, Lehmer R D, Mahdavi M A, Maingi R, Moyer R A, Petrie T W, Rognlien T D, Schaffer M J, Stambaugh R D, Wade M R, Watkins J G, West W P and Wolf N 1999 *Plasma Physics and Controlled Fusion* **41** A345–A355
- [19] Dunne M G, Potzel S, Reimold F, Wischmeier M, Wolfrum E, Frassinetti L, Beurskens M, Bilkova P, Cavedon M, Fischer R, Kurzan B, Laggner F M, McDermott R M, Tardini G, Trier E, Viezzer E, Willensdorfer M, Team T E M and Team T A U 2017 *Plasma Physics and Controlled Fusion* **59** 014017
- [20] Greenwald M, Terry J, Wolfe S, Ejima S, Bell M, Kaye S and Neilson G 1988 *Nuclear Fusion* **28** 2199
- [21] Pitts R A, Kukushkin A, Loarte A, Martin A, Merola M,

- Kessel C E, Komarov V and Shimada M 2009 *Physica Scripta* **T138** 014001
- [22] Soukhanovskii V A 2017 *Plasma Physics and Controlled Fusion* **59** 064005
- [23] Wenninger R, Bernert M, Eich T, Fable E, Federici G, Kallenbach A, Loarte A, Lowry C, McDonald D, Neu R, Pütterich T, Schneider P, Sieglin B, Strohmayer G, Reimold F and Wischmeier M 2014 *Nuclear Fusion* **54** 114003
- [24] Bernert M, Wischmeier M, Huber A, Reimold F, Lipschultz B, Lowry C, Brezinsek S, Dux R, Eich T, Kallenbach A, Lebschy A, Maggi C, McDermott R, Pütterich T and Wiesen S 2017 *Nuclear Materials and Energy* **12** 111 – 118 ISSN 2352-1791 proceedings of the 22nd International Conference on Plasma Surface Interactions 2016, 22nd PSI
- [25] Coda S, Ahn J, Albanese R, Alberti S, Alessi E, Allan S, Anand H, Anastassiou G, Andrèbe Y, Angioni C, Ariola M, Bernert M, Beurskens M, Bin W, Blanchard P, Blanken T, Boedo J, Bolzonella T, Bouquey F, Braunmüller F, Bufferand H, Buratti P, Calabró G, Camenen Y, Carnevale D, Carpanese F, Causa F, Cesario R, Chapman I, Chellai O, Choi D, Cianfarani C, Ciraolo G, Citrin J, Costea S, Crisanti F, Cruz N, Czarnecka A, Decker J, Masi G D, Tommasi G D, Douai D, Dunne M, Duval B, Eich T, Elmore S, Esposito B, Faitsch M, Fasoli A, Fedorczak N, Felici F, Février O, Ficker O, Fietz S, Fontana M, Frassinetti L, Furno I, Galeani S, Gallo A, Galperti C, Garavaglia S, Garrido I, Geiger B, Giovannozzi E, Gobbin M, Goodman T, Gorini G, Gospodarczyk M, Granucci G, Graves J, Guirlet R, Hakola A, Ham C, Harrison J, Hawke J, Hennequin P, Hnat B, Hogewey D, Hogge J P, Honoré C, Hopf C, Horáček J, Huang Z, Igochine V, Innocente P, Schrittwieser C I, Isliker H, Jacquier R, Jardin A, Kamleitner J, Karpushov A, Keeling D, Kirneva N, Kong M, Koubiti M, Kovacic J, Krämer-Flecken A, Krawczyk N, Kudlacek O, Labit B, Lazzaro E, Le H, Lipschultz B, Llobet X, Lomanowski B, Loschiavo V, Lunt T, Maget P, Maljaars E, Malygin A, Maraschek M, Marini C, Martin P, Martin Y, Mastrostefano S, Maurizio R, Mavridis M, Mazon D, McAdams R, McDermott R, Merle A, Meyer H, Militello F, Miron I, Cabrera P M, Moret J M, Moro A, Moulton D, Naulin V, Nespoli F, Nielsen A, Nocente M, Nouailletas R, Nowak S, Odstrčil T, Papp G, Papřok R, Pau A, Pautasso G, Ridolfini V P, Piovesan P, Piron C, Pisokas T, Porte L, Preynas M, Ramogida G, Rapson C, Rasmussen J J, Reich M, Reimerdes H, Reux C, Ricci P, Rittich D, Riva F, Robinson T, Saarelma S, Saint-Laurent F, Sauter O, Scannell R, Schlatter C, Schneider B, Schneider P, Schrittwieser R, Sciortino F, Sertoli M, Sheikh U, Sieglin B, Silva M, Sinha J, Sozzi C, Spolaore M, Stange T, Stoltzfus-Dueck T, Tamain P, Teplukhina A, Testa D, Theiler C, Thornton A, Tophøj L, Tran M, Tsironis C, Tsui C, Uccello A, Vartanian S, Verdoolaege G, Verhaegh K, Vermare L, Vianello N, Vijvers W, Vlahos L, Vu N, Walkden N, Wauters T, Weisen H, Wischmeier M, Zestanakis P, Zuin M and the EUROfusion MST1 team 2017 *Nuclear Fusion* **57** 102011
- [26] Wiesen S, Reiter D, Kotov V, Baelmans M, Dekeyser W, Kukushkin A, Lisgo S, Pitts R, Rozhansky V, Saibene G, Veselova I and Voskoboinikov S 2015 *Journal of Nuclear Materials* **463** 480 – 484 ISSN 0022-3115 plasma-surface interactions 21
- [27] Bufferand H, Ciraolo G, Marandet Y, Bucalossi J, Ghendrih P, Gunn J, Mellet N, Tamain P, Leybros R, Fedorczak N, Schwander F and Serre E 2015 *Nuclear Fusion* **55** 053025
- [28] Theiler C, Harrison J, Février O, De Oliveira H, Bernert M, Boedo J, Duval B, Fedorczak N, Fil A, Galassi D, Gallo A, Innocente P, Labit B, Linehan B, Lipschultz B, Maurizio R, Mumgaard B, Perek A, Reimerdes H, Sheikh U, Thornton A, Tsui C, Verhaegh K, Vianello N, Vijvers W, Wensing M and Wüthrich C 2018 SOL transport and detachment in alternative divertor configurations in TCV L- and H-mode plasmas *Proc. 27th IAEA Fusion Energy Conference, Gandhinagar, India, October 22-27* pp paper EX/P1-19
- [29] Harrison J R, Theiler C, Février O, de Oliveira H, Maurizio R, Verhaegh K, Perek A, Karpushov A, Lipschultz B, Duval B P, Feng X, Henderson S, Labit B, Linehan B, Merle A, Reimerdes H, Sheikh U, Tsui C K, Vijvers W A J, Wüthrich C and and 2019 *Plasma Physics and Controlled Fusion* **61** 065024
- [30] Bates S C and Burrell K H 1984 *Review of Scientific Instruments* **55** 934–939
- [31] Pitts R, Duval B, Loarte A, Moret J M, Boedo J, Coster D, Furno I, Horacek J, Kukushkin A, Reiter D and Rommers J 2001 *Journal of Nuclear Materials* **290** 940 – 946 ISSN 0022-3115 14th Int. Conf. on Plasma-Surface Interactions in Controlled Fusion Devices
- [32] Février O, Theiler C, Oliveira H D, Labit B, Fedorczak N and Baillo A 2018 *Review of Scientific Instruments* **89** 053502
- [33] De Oliveira H, Marmillod P, Theiler C, Chavan R, Février O, Labit B, Lavanchy P, Marlétaz B and Pitts R A 2019 *Review of Scientific Instruments* **90** 083502
- [34] Verhaegh K, Lipschultz B, Duval B, Harrison J, Reimerdes H, Theiler C, Labit B, Maurizio R, Marini C, Nespoli F, Sheikh U, Tsui C, Vianello N and Vijvers W 2017 *Nuclear Materials and Energy* **12** 1112 – 1117 ISSN 2352-1791 proceedings of the 22nd International Conference on Plasma Surface Interactions 2016, 22nd PSI
- [35] Hawke J, Andrebe Y, Bertizzolo R, Blanchard P, Chavan R, Decker J, Duval B, Lavanchy P, Llobet X, Marlétaz B, Marmillod P, Pochon G and Toussaint M 2017 *Journal of Instrumentation* **12** C12005
- [36] Maurizio R, Elmore S, Fedorczak N, Gallo A, Reimerdes H, Labit B, Theiler C, Tsui C, Vijvers W, Team T T and Team T M 2017 *Nuclear Fusion* **58** 016052
- [37] Kamleitner J 2015 *Suprathermal electron studies in Tokamak plasmas by means of diagnostic measurements and modeling* Ph.D. thesis École Polytechnique Fédérale de Lausanne École Polytechnique Fédérale de Lausanne
- [38] Linehan B L, Mumgaard R T, Wensing M, Verhaegh K, Andrebe Y, Harrison J R, Duval B P and Theiler C 2018 *Review of Scientific Instruments* **89** 103503
- [39] Vijvers W, Mumgaard R, Andrebe Y, Classen I, Duval B and Lipschultz B 2017 *Journal of Instrumentation* **12** C12058
- [40] Perek A, Vijvers W, Andrebe Y, Classen I, Duval B, Galperti C, Harrison J R, Linehan B L, Ravensbergen T, Verhaegh K and de Baar M MANTIS: a real-time quantitative multispectral imaging system for fusion plasmas. to be submitted
- [41] Silburn S URL <https://github.com/euratom-software/calcam>
- [42] Harrison J, Vijvers W, Theiler C, Duval B, Elmore S, Labit B, Lipschultz B, van Limpt S, Lisgo S, Tsui C, Reimerdes H, Sheikh U, Verhaegh K and Wischmeier M 2017 *Nuclear Materials and Energy* **12** 1071 – 1076 ISSN 2352-1791 proceedings of the 22nd International Conference on Plasma Surface Interactions 2016, 22nd PSI
- [43] Boedo J A, Crocker N, Chousal L, Hernandez R, Chalfant J, Kugel H, Roney P and Wertenbaker J 2009 *Review of Scientific Instruments* **80** 123506
- [44] Tsui C K, Boedo J A, Myra J R, Duval B, Labit B, Theiler C, Vianello N, Vijvers W A J, Reimerdes H, Coda S, Février O, Harrison J R, Horacek J, Lipschultz B, Maurizio R, Nespoli F, Sheikh U, Verhaegh K and

- Walkden N 2018 *Physics of Plasmas* **25** 072506
- [45] Sauter O, Angioni C and Lin-Liu Y R 1999 *Physics of Plasmas* **6** 2834–2839
- [46] Sauter O, Angioni C and Lin-Liu Y R 2002 *Physics of Plasmas* **9** 5140–5140
- [47] Harrison J 2001 *Characterisation of Detached Plasmas on the MAST Tokamak* Ph.D. thesis University of York
- [48] Reimerdes H, Canal G P, Duval B P, Labit B, Lunt T, Vijvers W A J, Coda S, Temmerman G D, Morgan T W, Nespoli F and B T 2013 *Plasma Physics and Controlled Fusion* **55** 124027
- [49] Weinlich M and Carlson A 1997 *Physics of Plasmas* **4** 2151–2160
- [50] Stangeby P C 1987 *Journal of Physics D: Applied Physics* **20** 1472–1478
- [51] Fil A, Dudson B, Lipschultz B, Moulton D, Verhaegh K, Fevrier O, Wensing M, teams E M and team T T 2018 *Contributions to Plasma Physics* **58** 746–750
- [52] Sheikh U A, Duval B P, Labit B and Nespoli F 2016 *Review of Scientific Instruments* **87** 11D431
- [53] Reimold F, Wischmeier M, Bernert M, Potzel S, Kallenbach A, Müller H, Sieglin B and U S 2015 *Nuclear Fusion* **55** 033004
- [54] Pitts R, Refke A, Duval B, Furno I, Joye B, Lister J, Martin Y, Moret J M, Rommers J and Weisen H 1999 *Journal of Nuclear Materials* **266-269** 648 – 653 ISSN 0022-3115
- [55] Ravensbergen T, van Berkel M, Silburn S, Harrison J, Perek A, Vijvers W, Theiler C, Kirk A, de Baar M, team T E M and the TCV team Real-time detection of the emission front during divertor detachment using multi-spectral imaging. to be submitted
- [56] Van Berkel M, Ravensbergen T, Perek A, Galperti C, Van Kampen R, Lammers J, Fevrier O, Henderson S, Komm M, Brida D *et al.* 2019 *Bulletin of the American Physical Society*
- [57] Tsui C K, Boedo J A, Halpern F D, Loizu J, Nespoli F, Horacek J, Labit B, Morales J, Reimerdes H, Ricci P, Theiler C, Coda S, Duval B P and Furno I 2017 *Physics of Plasmas* **24** 062508
- [58] Kallenbach A, Asakura N, Kirk A, Korotkov A, Mahdavi M, Mossessian D and Porter G 2005 *Journal of Nuclear Materials* **337-339** 381 – 385 ISSN 0022-3115 pSI-16
- [59] Stangeby P, Canik J, Elder J, Lasnier C, Leonard A, Eldon D, Makowski M, Osborne T and Grierson B 2015 *Nuclear Fusion* **55** 093014
- [60] Fevrier O, Theiler C, Tsui C K, Verhaegh K, Maurizio R, Labit B, Reimerdes H, Duval B, Boedo J A, Lipschultz B, Tcv Team and Eurofusion Mst1 Team 2017 Evolution of pressure drop during detachment in the TCV tokamak *APS Meeting Abstracts* p PP11.075
- [61] Kallenbach A, Sun H J, Eich T, Carralero D, Hobirk J, Scarabosio A, Siccino M and and 2018 *Plasma Physics and Controlled Fusion* **60** 045006
- [62] Kallenbach A, Bernert M, Dux R, Eich T, Henderson S, Pütterich T, Reimold F, Rohde V and Sun H 2019 *Nuclear Materials and Energy* **18** 166 – 174 ISSN 2352-1791
- [63] Schneider R, Bonnin X, Borrass K, Coster D P, Kastelewicz H, Reiter D, Rozhansky V A and Braams B J 2006 *Contributions to Plasma Physics* **46** 3–191 ISSN 1521-3986
- [64] Pitcher C S and Stangeby P C 1997 *Plasma Physics and Controlled Fusion* **39** 779–930
- [65] Garcia O, Horacek J, Pitts R, Nielsen A, Fundamenski W, Naulin V and Rasmussen J J 2007 *Nuclear Fusion* **47** 667–676
- [66] Vianello N, Tsui C, Theiler C, Allan S, Boedo J, Labit B, Reimerdes H, Verhaegh K, Vijvers W, Walkden N, Costea S, Kovacic J, Ionita C, Naulin V, Nielsen A, Rasmussen J J, Schneider B, Schrittwieser R, Spolaore M, Carralero D, Madsen J, Lipschultz B, Militello F, The TCV Team and The EUROfusion MST1 Team 2017 *Nuclear Fusion* **57** 116014
- [67] Vianello N, Carralero D, Tsui C K, Naulin V, Agostini M, Cziegler I, Labit B, Theiler C, Aguiam D, Allan S, MBernert, Boedo J, Costea S, Oliveira H D, F’evrier O, Galdon-Quiroga J, Grenfell G, Hakola A, Ionita C, Isliker H, Karpushov A, Kovacic J, Lipschultz B, Maurizio R, McClements K, Militello F, Nielsen A J, Olsen J, Rasmussen J J, Ravensbergen T, Reimerdes H, Schneider B, Schrittwieser R, Seliunin E, Spolaore M, Verhaegh K, Vicente J, Walkden N, Zhang W, Wolfrum E, the ASDEX Upgrade Team, the TCV Team and the EUROfusion MST1 Team Scrape Off Layer (SOL) transport and filamentary dynamics in high density tokamak regimes. submitted
- [68] LaBombard B, Boivin R L, Greenwald M, Hughes J, Lipschultz B, Mossessian D, Pitcher C S, Terry J L and Zweben S J 2001 *Physics of Plasmas* **8** 2107–2117
- [69] Kuang A, LaBombard B, Brunner D, Garcia O, Kube R and Theodorsen A 2019 *Nuclear Materials and Energy* **19** 295 – 299 ISSN 2352-1791
- [70] McCormick K, Kyriakakis G, Neuhauser J, Kakoulidis E, Schweinzer J and Tsois N 1992 *Journal of Nuclear Materials* **196-198** 264 – 270 ISSN 0022-3115 plasma-Surface Interactions in Controlled Fusion Devices
- [71] Carralero D, Birkenmeier G, Müller H, Manz P, deMarne P, Müller S, Reimold F, Stroth U, Wischmeier M and E W 2014 *Nuclear Fusion* **54** 123005
- [72] Rudakov D, Boedo J, Moyer R, Stangeby P, Watkins J, Whyte D, Zeng L, Brooks N, Doerner R, Evans T, Fenstermacher M, Groth M, Hollmann E, Krashenninikov S, Lasnier C, Leonard A, Mahdavi M, McKee G, McLean A, Pigarov A, Wampler W, Wang G, West W and Wong C 2005 *Nuclear Fusion* **45** 1589–1599
- [73] Wynn A, Lipschultz B, Cziegler I, Harrison J, Jaervinen A, Matthews G F, Schmitz J, Tal B, Brix M, Guillemaut C, Frigione D, Huber A, Joffrin E, Kruzei U, Militello F, Nielsen A, Walkden N, Wiesen S and Contributors J 2018 *Nuclear Fusion* **58** 056001
- [74] Asakura N, Koide Y, Itami K, Hosogane N, Shimizu K, Tsuji-Iio S, Sakurai S and Sakasai A 1997 *Journal of Nuclear Materials* **241-243** 559 – 563 ISSN 0022-3115
- [75] Moret J M, Buhlmann F and Tonetti G 2003 *Review of Scientific Instruments* **74** 4634–4643
- [76] Stangeby P and Chanin A 1996 *Nuclear Fusion* **36** 839–852
- [77] Guo H, Wang H, Watkins J, Casali L, Covele B, Moser A, Osborne T, Samuell C, Shafer M, Stangeby P, Thomas D, Boedo J, Buttery R, Groebner R, Hill D, Holland L, Hyatt A, Jaervinen A, Kellman A, Lao L, Lasnier C, Leonard A, Murphy C, Ren J, Sang C, Sontag A and T T 2019 *Nuclear Fusion* **59** 086054
- [78] Jaervinen A E, Allen S L, Eldon D, Fenstermacher M E, Groth M, Hill D N, Leonard A W, McLean A G, Porter G D, Rognlén T D, Samuell C M and Wang H Q 2018 *Phys. Rev. Lett.* **121**(7) 075001 URL <https://link.aps.org/doi/10.1103/PhysRevLett.121.075001>
- [79] Loarte A, Monk R D, Kukushkin A S, Righi E, Campbell D J, Conway G D and Maggi C F 1999 *Phys. Rev. Lett.* **83**(18) 3657–3660
- [80] Huber A, Rapp J, Andrew P, Coad P, Corrigan G, Erents K, Fundamenski W, Ingesson L, Jachmich S, Korotkov A, Matthews G, Mertens P, Philipps V, Pitts R, Schweer B, Sergienko G and Stamp M 2005 *Journal of Nuclear Materials* **337-339** 241 – 245 ISSN 0022-3115 pSI-16
- [81] Christen N, Theiler C, Rognlén T, Rensink M, Reimerdes H, Maurizio R and Labit B 2017 *Plasma Physics and Controlled Fusion* **59** 105004
- [82] Fil A, Moulton D, Dudson B, Lipschultz B, Verhaegh K,

- Fevrier O, Myatra O, Theiler C, Wensing M, teams E M and team T T 2019 *submitted to Plasma Physics and Controlled Fusion*
- [83] Reimold F, Wischmeier M, Potzel S, Guimaraes L, Reiter D, Bernert M, Dunne M and Lunt T 2017 *Nuclear Materials and Energy* **12** 193 – 199 ISSN 2352-1791 proceedings of the 22nd International Conference on Plasma Surface Interactions 2016, 22nd PSI
- [84] Aho-Mantila L, Potzel S, Coster D P, Wischmeier M, Brix M, Fischer R, Marsen S, Meigs A, Müller H W, Scarabosio A, Stamp M F and Brezinsek S 2017 *Plasma Physics and Controlled Fusion* **59** 035003
- [85] Dekeyser W, Bonnin X, Lisgo S, Pitts R, Brunner D, LaBombard B and Terry J L 2017 *Nuclear Materials and Energy* **12** 899 – 907 ISSN 2352-1791 proceedings of the 22nd International Conference on Plasma Surface Interactions 2016, 22nd PSI
- [86] Hutchinson I H, LaBombard B, Goetz J A, Lipschultz B, McCracken G M, Snipes J A and Terry J L 1995 *Plasma Physics and Controlled Fusion* **37** 1389–1406